1 **Mitochondrial fission is increased in macrophages during mROS production in response to**
2 ***S. pneumoniae***
3

4 Mohammed Mohasin[a,b,*], Katharin Balbirnie-Cumming[c] Emily Fisk[a,b], Elizabeth C. Prestwich[a],
5 Clark D. Russell[c], Jennifer Marshall[c], Clare Pridans[c], Scott P. Allen[d], Pamela J. Shaw[d], Kurt J.
6 De Vos[d,e], Christopher J. Hill[f], Per Bullough[b,g], Alison M. Condliffe[a,b], Tim J. Mitchell[h], Helen
7 M. Marriott[a,b,e], David H. Dockrell[c,#]
8 [a]Department of Infection, Immunity and Cardiovascular Disease, University of Sheffield
9 Medical School, UK
10 [b]The Florey Institute for Host-Pathogen Interactions, University of Sheffield Medical School,
11 UK
12 [c]Department of Infection Medicine and MRC Centre for Inflammation Research, University of
13 Edinburgh, UK
14 [d]Department of Neuroscience, Sheffield Institute for Translational Neuroscience, University of
15 Sheffield Medical School, UK
16 [e]Centre for Membrane Interactions and Dynamics, Department of Molecular Biology and
17 Biotechnology, University of Sheffield, UK
18 [f]Department of Biomedical Science, Department of Molecular Biology and Biotechnology,
19 University of Sheffield, UK
20 [g]Krebs Institute, Department of Molecular Biology and Biotechnology, University of Sheffield,
21 UK
22 [h]Institute of Microbiology and Infection, School of Immunity and Infection, University of
23 Birmingham, UK

24 * Present Address: Department of Biochemistry and Molecular Biology, University of Dhaka,

25 Bangladesh

26

27 **Requests for reprints:** David H. Dockrell Department of Infection Medicine and MRC Centre

28 for Inflammation Research, University of Edinburgh, UK

29 Email: david.dockrell@ed.ac.uk

30

31 **#Corresponding Author:** David H. Dockrell

32 Phone: +44 (0) 131 242 6581

33 Fax: +44 (0) 131 242 6578

34 Email: david.dockrell@ed.ac.uk

35

36 **Running title:** innate macrophage mitochondrial fission

37 Word count: Abstract: 159

38 Main text: 6,184

39

ABSTRACT

Immunometabolism and regulation of mitochondrial reactive oxygen species (mROS) are critical determinants of the immune effector phenotype of differentiated macrophages. Mitochondrial function requires dynamic fission and fusion, but whether effector function is associated with altered dynamics during bacterial responses is unknown. We show that macrophage mitochondria undergo fission after 12 h of progressive ingestion of live *Streptococcus pneumoniae* (pneumococci). Fission is associated with progressive reduction in oxidative phosphorylation but increased mROS generation. Fission is enhanced by mROS production, PI3Kγ signaling and by cathepsin B, but not by inflammasome activation or IL-1β generation. Reduced fission following PI3Kγ or cathepsin B inhibition is associated with reduced mROS generation and bacterial killing. Fission is associated with Parkin recruitment to mitochondria, but not mitophagy. Fission occurs upstream of apoptosis induction and independently of caspase activation. During macrophage innate responses to live bacteria mitochondria shift from oxidative phosphorylation and ATP generation to mROS production and microbicidal responses with a progressive shift towards mitochondrial fission.

60 **INTRODUCTION**

61 Macrophages are an essential component of innate immune responses to pathogenic bacteria (1).
62 Pathogen clearance by macrophages involves a co-ordinated response requiring phagocytosis of
63 bacteria, generation of microbicidals and orchestration of the inflammatory response via
64 cytokine/chemokine networks. Macrophage activation results from activation of diverse pattern
65 recognition receptors by microbial products (2, 3). Our understanding of the exact microbicidal
66 strategies utilized by macrophages against extracellular bacteria is still incomplete but we have
67 recently shown that mitochondrial reactive oxygen species (mROS) are an integral part of the
68 anti-bacterial response required to clear *Streptococcus pneumoniae* (pneumococci) (4). *S.*
69 *pneumoniae* remains the leading cause of bacterial community-acquired pneumonia (CAP) and is
70 a significant cause of bacteraemia and meningitis (2). Host-pathogen interactions between
71 pneumococci and differentiated macrophages provides an informative model for the interaction
72 between extracellular encapsulated bacteria and tissue macrophages (1).
73
74 Mitochondria play key roles in innate host defence and contribute to pathogen sensing, cytokine
75 production and pathogen clearance (5, 6). In particular, mitochondria have emerged as critical
76 effectors of delayed-phase microbicidal responses to ingested bacteria, through generation of
77 mROS (4, 7, 8). The emerging area of immunometabolism links metabolic pathway utilization to
78 effector phenotype and has been particularly informative in defining mechanisms underpinning
79 macrophage responses to microbial stimuli (9). Mitochondrial function is regulated by dynamics
80 with a balance between fission and fusion essential for optimal function (10). To date there has
81 been little exploration of how mitochondrial dynamics are altered during microbicidal responses
82 and increased production of mROS. A shift to glycolytic metabolism is associated with

83 mitochondrial fission (11, 12). This is noteworthy since the shift to glycolytic metabolism is
84 recognised as a critical determinant in shaping macrophage activation and innate immune
85 effector function in response to pattern recognition receptor (PRR) stimulation by pathogen-
86 associated molecular patterns (PAMPs) such as LPS (13-15). There is, however, limited
87 understanding of immunometabolic responses and changes in mitochondrial dynamics during
88 challenge with live bacteria, as opposed to microbial components, and how these relate to mROS
89 generation and bacterial killing.
90
91 We demonstrate that the host response to pneumococci in macrophages involves induction of
92 fission in response to live bacteria. Fission is associated with reduced oxidative phosphorylation
93 but enhanced mROS production, which promotes fission. Inhibition of phosphoinositide 3-kinase
94 (PI3K) signalling and cathepsin B reduce mitochondrial fission and intracellular bacterial killing.
95 Fission leads to Parkin activation but is not associated with mitophagy and occurs upstream of
96 apoptosis induction. Overall this suggests mitochondrial fission is contemporaneous with
97 mitochondrial adaption to microbicidal function following ingestion of bacteria. (This article was
98 submitted to an online preprint archive (16)).
99

100 **RESULTS**

101 **Sustained bacterial exposure results in increased mitochondrial fission in macrophages.**

102 We have previously shown that differentiated macrophages have an extensive mitochondrial
103 volume in comparison to less differentiated monocytes and macrophages (17). As shown in Fig.
104 1A-C, the mitochondrial network showed extensive branch-points in mock-infected BMDM but,
105 in contrast, showed limited complexity after extended bacterial challenge, using a previously
106 developed algorithm for the calculation of branch points (18) as illustrated in Fig. S1. Analysis
107 of the kinetics of this response showed increased mitochondrial fission was a response that
108 progressed over time and was significant by 12-14 h following bacterial challenge (Fig. 1D).
109 When we looked at mitochondrial ultrastructure in BMDM we also noted reduction in cristae
110 following bacterial challenge (Fig. 1E-F).

111

112 **Mitochondrial fission is a response to live bacteria.**

113 Prior reports have described Drp-1 independent mitochondrial fission in HeLa cells containing
114 *Listeria monocytogenes* (19). In this model fission was induced by the cholesterol-dependent
115 cytolysin (CDC), listeriolysin O, as well as by related CDCs, including pneumolysin expressed
116 by pneumococci, but occurred rapidly after exposure and was transient in duration (20). We
117 addressed the microbiologic requirements for the delayed fission we observed in macrophages.
118 Live bacteria induced fission, but heat-killed bacteria did not (Fig. 2). A pneumolysin deficient
119 mutant at a comparable MOI to the wild-type strain induced lower levels of mitochondrial
120 fission, but by increasing the MOI of the pneumolysin deficient mutant we were able to
121 reconstitute mitochondrial fission to comparable levels, despite absence of the toxin. Exogenous

122 pneumolysin also induced mitochondrial fission only in association with higher lytic
123 concentrations, as confirmed by red blood cell lysis assay (21).

124

125 Collectively this suggested that although pneumolysin contributes to mitochondrial fission it is
126 not essential. This therefore emphasised some important features of fission in macrophages
127 responding to live bacteria as opposed to prior reports in other cell types (20). In particular it
128 suggested that in macrophages mitochondrial fission was a response to a bacterial pathogen we
129 have previously shown is contained within the phagolysosome (4), and did not have an absolute
130 requirement for expression of a CDC. This raised the possibility that it arose as a host response
131 to live bacteria.

132

133 **Mitochondrial fission is associated with altered mitochondrial metabolism.**

134 We next investigated whether fission induced by challenge with live bacteria was associated with
135 changes in cell metabolism, since prior reports suggest reduction of oxidative phosphorylation is
136 associated with enhanced mitochondrial fission (22). Extracellular acidification was enhanced
137 following bacterial exposure (Fig. S2A-B). Basal oxygen consumption (OCR) rate was not
138 significantly altered by bacteria (Fig. S2C) but maximal and ATP linked OCR were reduced after
139 pneumococcal challenge (Fig. 3A-D), as was respiration reserve (Fig. S2D). Moreover, proton
140 leakage (Fig. 3E) and non-mitochondrial OCR (Fig. S2E) were increased by pneumococcal
141 challenge. These findings were also confirmed in human monocyte-derived macrophages
142 (MDM), with confirmation of increased ECAR early after bacterial challenge (Fig. S3A). In
143 addition, a reduction in maximal and ATP-linked (but not basal) OCR and an increase in proton

144 leakage was apparent after bacterial challenge (Fig. S3B-G). Although the shift to glycolytic
145 metabolism was apparent by 4 h the changes in maximal OCR and proton leak were only
146 apparent at the later 16 h time point after bacterial challenge (Fig. S3B-G). Proton leak is often a
147 step designed to limit mROS production when mROS generation is high (23) and in association
148 with this we observed increased mROS generation (Fig. 3F-G). The reductions in maximal and
149 ATP-linked OCR after bacterial challenge were reduced in the presence of mitoTEMPO, an
150 inhibitor of mROS (24), whereas the increases in glycolytic metabolism and non-mitochondrial
151 OCR were not altered (Fig. 3B-D and Fig. S2). Since enhanced mROS generation was a
152 prominent response and contributed to the reduction in changes in OCR we also tested to what
153 extent fission was a direct result of mROS production and documented that mROS inhibition
154 reduced mitochondrial fission after bacterial challenge (Fig. 3H-I). Collectively these results
155 showed that enhanced mitochondrial fission following pneumococcal challenge is associated
156 with a decline in oxidative phosphorylation and an increase in mROS generation. Of note, mROS
157 directly contributes to mitochondrial fission and the alteration in oxidative phosphorylation,
158 while the delayed emergence of the altered parameters of oxidative phosphorylation matches the
159 delayed kinetics of mitochondrial fission.

160

161 **PI3K regulates early mitochondrial fission and macrophage microbicidal responses.**

162 We next addressed factors which regulate fission. Since fission was associated with live bacteria
163 and mROS production we hypothesized that responses linking pathogen sensing to mROS
164 expression in macrophages could contribute. Phosphatidylinositol 3-kinase (PI3K) signalling
165 enhances mROS production in response to microbial factors in macrophages (25) and is

166 activated by a range of microbial stimuli (26). In line with this we observed that while
167 pneumococcal challenge significantly increased mROS generation that in the presence of pan-
168 PI3K inhibitors, mROS levels were lower and were not significantly increased with LY294002
169 (Pan-PI3Ki) as compared to the pneumococcal challenge with vehicle control at any time point
170 (Fig. 4A-B). We next addressed if a particular PI3K isoform was associated with regulation of
171 fission and observed significant inhibition of mROS with the PI3Kγ isoform, an isoform highly
172 expressed in macrophages (27), albeit to a slightly lower degree than with the pan-PI3K
173 inhibitors (Fig. 4A and C). The pan-PI3K inhibitor completely blocked fission while the PI3Kγ
174 isoform partially blocked fission (Fig. 4D-F). In keeping with microbicidal roles for mROS in
175 delayed microbicidal responses to pneumococci (4), pan-PI3K and PI3Kγ isoform selective
176 inhibitors reduced bacterial killing, with a numerically greater fold increase in viable
177 intracellular bacteria apparent with the pan-PI3K inhibitor (Fig. 4G-H).

178

179 **Cathepsin B regulates early mitochondrial fission and macrophage microbicidal responses.**

180 Prolonged exposure to internalized bacteria and mROS leads to lysosomal membrane
181 permeabilization and cathepsin activation (21, 28). Cathepsin B can also stimulate mROS
182 production from mitochondria (29). Lysosomal membrane permeabilization has been linked to
183 mitochondrial fission (30) and we next addressed whether cathepsin B influenced mitochondrial
184 fission. As predicted two separate cathepsin B inhibitors reduced mROS production (Fig.5A-D),
185 but also fission (Fig. 5E-H). In keeping with these findings, both cathepsin B inhibitors also
186 increased viable intracellular bacteria (Fig. 5I-J). The impact of two cathepsin inhibitors on
187 TNFα generation varied from no inhibition to partial inhibition but the effect of cathepsin B

188 inhibitors on generation of IL-1β was more marked with inhibition of greater extent than that
189 observed for TNFα (Fig. S4A-B), in line with previous observations (31). Inhibition of mROS
190 also completely blocked IL-1β production but had no impact on production of TNF-α from
191 macrophages. Since mROS contributes to inflammasome activation resulting in IL-
192 1β generation (28), we also questioned whether inflammasome activation or IL-1β signalling
193 mediated mitochondrial fragmentation and might feedback to mediate the fission associated with
194 mROS or cathepsin B activation. However, the caspase-1 inhibitor YVAD and IL-1RA did not
195 modify mitochondrial fission (Fig. S4C-D).

196 Overall this demonstrated that mROS production and mitochondrial fission were regulated by
197 PI3K signalling and by cathepsin B upstream of mROS roles on inflammasome activation or IL-
198 1β production.

199

200 **Mitochondrial fission following bacterial challenge is associated with recruitment of Parkin**
201 **upstream of apoptosis induction.**

202 Having documented that macrophages responding to live pneumococci undergo mitochondrial
203 fission and upregulate mROS production we next examined what the consequences of these
204 processes were to mitochondrial homeostasis. High levels of mROS result in alterations to
205 mitochondrial proteins, which evokes a number of responses including activation of the PINK-
206 1/Parkin system (10). Parkin is an E3 ligase which ubiquitinates damaged mitochondrial proteins
207 to activate their removal via the 26S proteasome system. We found a marked increase in Parkin
208 expression and co-localization of Parkin with mitochondria following bacterial challenge (Fig.
209 6A-C). In association with this we also observed increased Parkin in the mitochondrial fraction

210 of cells after bacterial challenge (Fig. S5A-C). Since extensive damage to mitochondria can
211 trigger removal by mitophagy (10), we next examined if there was any evidence of mitophagy in
212 macrophages challenged with pneumococci. As shown in Fig. S5D, we found no evidence of
213 activation of the autophagy maker LC3B, although this was induced in macrophages exposed to
214 the mitochondrial oxidative phosphorylation uncoupler Carbonyl cyanide 4-
215 (trifluoromethoxy)phenylhydrazone (FCCP), and also found no evidence for mitophagy
216 associated double-membrane containing vacuoles by transmission electron microscopy (Fig.
217 S5E).

218 Although a downstream consequence of sustained phagocytosis and bacterial killing is induction
219 of apoptosis, which further increases mROS-dependent killing through caspase-dependent
220 mechanisms (4, 8, 32), we found no evidence of apoptosis when mitochondrial fission was
221 initially observed at the 12 h time point (Fig. S6A-B). Furthermore, a pan-caspase inhibitor
222 zVAD-fmk, which blocks apoptosis-dependent caspases had no impact on fission (Fig. 6D-E),
223 suggesting that mitochondrial fission was upstream of apoptosis induction. Consistent with this,
224 examination of mitochondrial morphology showed that in apoptotic cells mitochondria became
225 swollen and looked similar to those noted after FCCP treatment (compare Fig. S6A with Fig.
226 S5D), while the appearance at the stages prior to apoptosis, at 12-14 h, were characterized by
227 shortening and lack of branching but not by swelling. In addition, loss of inner mitochondrial
228 transmembrane potential ($\Delta\psi_m$), a feature of activation of the mitochondrial pathway of
229 apoptosis after pneumococcal challenge (21), was only apparent at relatively low levels at 12 h
230 after bacterial challenge, in contrast to levels at later time points (Fig. S6C-D). This
231 demonstrated that although the recruitment of Parkin was associated with early signs of loss of

232 $\Delta\psi_m$ it preceded induction of high levels or advanced stages of apoptosis with caspase activation
233 and occurred early after fission commenced, prior to commitment to apoptosis.

234

235 **DISCUSSION**

236 We demonstrate that sustained internalization of live opsonized *S. pneumoniae* results in
237 increased mitochondrial fission in primary macrophages. This is a response that occurs as
238 macrophages reduce reliance on oxidative phosphorylation for ATP generation and as mROS
239 generation progressively increases. mROS, PI3K signalling and cathepsin B promote
240 mitochondrial fission which is associated with increased killing of intracellular bacteria.
241 Ultimately, mitochondrial fission is associated with Parkin activation upstream of apoptosis
242 induction.

243

244 Immunometabolism has emerged as a critical determinant of macrophage polarization and
245 phenotype (33). Mitochondrial regulation of macrophage immune function involves release of
246 mROS, which is critical to both pathogen sensing and microbicidal responses (7, 34).
247 Macrophages adapt electron transport chain assembly in response to recognition of live bacteria
248 with associated increases in IL-1β production and fumarate generation, which has been shown to
249 contribute to clearance of *Escherichia coli* and *Salmonella enterica* Typhimurium (35).

250

251 Reduced oxidative phosphorylation and increased glycolytic metabolism promote fission (11,
252 12). Conversely, a putative inhibitor of canonical mitochondrial fission (Mdivi-1) reduced the
253 LPS-induced shift to glycolytic metabolism in murine bone marrow-derived macrophages

254 (BMDM) but as recently highlighted this inhibitor may also directly target complex I and
255 therefore mROS production so does not conclusively establish whether fission is essential for the
256 observed shift in phenotype as opposed to alterations in mROS (36-38). Increased mROS
257 production also enhances fission (10), but fission promotes mROS generation in mitochondria,
258 further amplifying the loop between fission and mROS generation (12). In contrast to the role for
259 mROS in promoting inflammasome activation, fission has been reported to have more variable
260 impact on inflammasome activation. There are reports that it promotes (39, 40) but also inhibits
261 inflammasome activation (41, 42). The shift to glycolytic metabolism during the macrophage
262 host response to bacterial infection would be anticipated to promote mitochondrial fission,
263 reduce reliance on mitochondrial ATP generation and enhance mROS mediated innate immune
264 responses.
265
266 Although reports also suggest that microbial factors, in particular cholesterol-dependent
267 cytolysins, may stimulate fission in non-myeloid cells, including pneumolysin produced by *S.*
268 *pneumoniae* (19, 20), we found that although pneumolysin was a contributory factor, it was not
269 essential for fission. Thus, in macrophages it is live bacteria that promote the delayed
270 mitochondrial fission we observed, similar to the observations of Garaude and colleagues,
271 where transient electron transport chain adaptations involving a shift to complex II activity
272 enable microbicidal responses that also required live bacteria (35). In our case, however, the
273 adaption we observed was a delayed response that progressed over time. We found that PI3K
274 signalling, a known component of pathogen sensing pathways, and in particular the PI3Kγ
275 isoform which is highly expressed in macrophages, promoted fission (27, 43).
276 PI3Kγ contributes to leukocyte recruitment, activation and nicotinamide adenine dinucleotide

277 phosphate-dependent ROS generation (27, 43), and we suggest an additional role regulating
278 fission and mROS production. PI3K inhibition has also reduced mitochondrial fission in tumor
279 cells, although in this setting this was achieved in association with modulation of trafficking to
280 the cortical cytoskeleton and in association with mROS enhancement (44). We also identified
281 cathepsin B as a factor regulating mitochondrial fission. Cathepsin B is activated and released
282 during phagolysosomal membrane maturation following ingestion of pneumococci (21). It has
283 been shown to stimulate mROS production (29). Both mROS and cathepsin B contribute to
284 inflammasome activation (45, 46), but we found no evidence that caspase 1 activation, or
285 downstream IL-1β production, regulate mitochondrial fission, even though we confirmed
286 cathepsin B contributes to IL-1β release from macrophages. Therefore, we conclude that
287 mROS and cathepsin B induced inflammasome activation occurs downstream of regulation of
288 fission and inflammasome activation, and the resulting IL-1β generation does not form a
289 regulatory feedback loop influencing fission (see Fig. 6F).

290

291 A critical factor in fission in our model is mROS or pathways that enhance mROS production.
292 Oxidative stress is known to lead to formation of mitochondrial-derived vesicles and the release
293 of these from mitochondria is dependent on Parkin and PINK-1 (47). It therefore remains to be
294 proven whether the fission we observe which is associated with mROS and Parkin recruitment to
295 mitochondria is regulated by a similar pathway. Ultimately progressive mitochondrial fission and
296 oxidative stress will lead to loss of $\Delta\psi_m$ and dysfunctional mitochondria could activate
297 mitophagy (48) or mitochondrial pathways of apoptosis induction via cytochrome c release and
298 mitochondrial outer membrane permeabilization (MOMP) (49, 50). Both processes involve
299 PTEN (phosphatase and tensin homolog) induced putative kinase 1 (PINK1) and Parkin, and the

300 extent of loss of $\Delta\psi_m$ and activation of the E3 ligase Parkin determines whether cells undergo
301 mitophagy (51) or apoptosis (52). We observed no evidence of mitophagy, while we have
302 previously documented this model results in apoptosis in association with downregulation of
303 Mcl-1 via ubiquitination and proteasomal degradation (32). We have shown that cathepsin D
304 stimulates Mcl-1 ubiquitination via the E3 ligase MULE (53). Parkin is another potential
305 mediator of Mcl-1 ubiquitination (52). The extent of loss of $\Delta\psi_m$ in the face of sustained
306 oxidative stress during macrophage responses to live bacteria is likely to favour apoptosis over
307 mitophagy (21). Fission can occur as an early event in apoptosis (54) and occurs upstream of
308 caspase activation (55). Consistent with this, in our model fission was unaltered by caspase
309 inhibition. However, we found evidence that fission is regulated by specific factors (mROS and
310 cathepsin B), which we have previously demonstrated do not mediate macrophage apoptosis
311 during pneumococcal challenge (4, 53). This suggests that although fission and enhanced mROS
312 play a key role in macrophage microbicidal responses, through intracellular pathogen killing and
313 cytokine generation, they are not required for the execution phase of apoptosis, which proceeds
314 as a result of Mcl-1 downregulation and MOMP despite inhibition of mROS and mitochondrial
315 fission.
316

317 In conclusion, we suggest that sustained responses to internalized live bacteria shift
318 mitochondrial dynamics progressively in favour of fission in association with reduced oxidative
319 phosphorylation. This is both the result of mROS production but enables further mROS
320 generation which can enhance IL-1β production and enable microbicidal responses that limit
321 intracellular pathogen survival. Although *S. pneumoniae* is relatively resistant to the direct
322 effects of ROS and the initial effects of mROS may be indirect (56), the subsequent induction

323 of caspase-dependent apoptosis increases mROS generation and enables mROS to act in
324 combination with other microbicidal responses (4), while apoptosis effectively terminates pro-
325 inflammatory cytokine responses. The reliance of macrophages on mROS to effectively control
326 clearance of internalized bacteria requires an effective program that includes mitochondrial
327 fission and adapting mitochondrial function away from oxidative phosphorylation and ATP
328 generation to prioritize microbicidal function.

329

330

331

332 **MATERIALS AND METHODS**

333

334 **Ethics Statement.**

335 Peripheral blood mononuclear cells were isolated from whole blood donated by healthy
336 volunteers with written informed consent, and differentiated into monocyte derived macrophages
337 (MDMs), as approved by the South Sheffield Regional Ethics Committee (07Q2305) and by the
338 Edinburgh Accredited Medical Regional Ethics Committee (15-HV-013). Animal experiments
339 were performed in accordance with U.K. Government Home Office Regulations (Animals
340 (Scientific Procedures) Act 1986) under Project Licences PPL 40/3726 (Professor David H.
341 Dockrell) and PPL 70/8915 (Dr. Clare Pridans) and ethical approval was granted by the
342 University of Sheffield Local Ethical Review Panel and The University of Edinburgh's Protocols
343 and Ethics Committees respectively. The animal care and use protocols adhered to National
344 Centre for the Replacement, Refinement and Reduction of Animals in Research guidelines
345 (Responsibility in the use of animals in bioscience research, April 2019 and Animal Research:
346 Reporting of *In Vivo* experiments guidelines, June 2010).

347

348 **Bacteria and infection.**

349 Serotype 2 *S. pneumoniae* (D39 strain; NCTC 7466) and the pneumolysin deficient strain *S.*
350 *pneumoniae* (PLYSTOP D39) were cultured and stored as previously described (21, 57). In some
351 experiments bacteria were heat-inactivated by placing in water at 60°C for 40 min. Prior to
352 macrophage challenge bacteria were opsonized in RPMI (Sigma-Aldrich) containing either 10%

353 mouse immunized pooled serum or human immunized pooled serum with detectable levels of
354 anti-pneumococcal antibodies for bone marrow-derived macrophages (BMDMs) or human
355 monocyte-derived macrophages (MDMs), respectively. The multiplicity of infection (MOI) or
356 bacteria to macrophage ratio was 10 unless otherwise stated. Endotoxin-free pneumolysin was
357 produced by Prof. Tim Mitchell (University of Birmingham) and shown to be haemolytic in a
358 sheep red blood cell haemolytic assay as previously described, before incubation with
359 macrophages for 12 h at 0.5-5 μg/mL (21). Cultures were incubated for the indicated time before
360 analysis.

361

362 **Isolation and culture of macrophages.**

363 Mouse BMDM were obtained from C57BL/6 mouse femurs and tibias and differentiated by
364 culture of 0.5 x 10^6 cells per well in 24 well plates (Corning) on 13 x 13 mm cover slips (VWR
365 International), or alternatively in either T25 or T75 flasks (Corning), in Dulbecco's Modified
366 Eagle's Media DMEM;(Bio Whittaker®), Lonza) with 10% fetal calf serum (FCS) with low LPS
367 (HyClone, Thermo Scientific) and 10% conditioned L929 media as a source of CSF-1, as
368 described previously (1). Cells were plated at 2 x 10^6 cells and cultured in RPMI with 10% FCS
369 with low endotoxin levels (Lonza). After 14 d, macrophages were challenged with bacteria or
370 mock-infected and incubated for 1 h on ice, followed by 3 h at 37°C with 5% CO_2. After
371 washing three times with PBS, cells were incubated for the indicated time period at 37°C with
372 5% CO_2 before analysis.

373

374 In certain experiments, macrophages were incubated with one of the following reagents for 1 h
375 prior to bacterial challenge; 100 μM MitoTempo (Enzo Life) to inhibit mROS, 1 mM 3-
376 methyladenine (3MA) (Sigma), or 15 μM Ly294002 as pan-PI3K inhibitors, 10 μM A66 as a
377 PI3Kα inhibitor, 10 μM A560524 as a PI3Kγ inhibitor, 3 μM IC87114 as a PI3Kδ inhibitor, 50
378 μM *N*-benzyloxycarbonyl–Phe-Ala fluoromethyl ketone (zFA-fmk) (ApexBio) or 25 μM (L-3-
379 *trans*-(Propylcarbamyl) oxirane-2-carbonyl)-L-isoleucyl-L-proline (CA-074me) (Sigma) to
380 inhibit cathepsin B, 50 μM carbobenzoxy-valyl-alanyl-aspartyl-[O-methyl]-fluoromethyl ketone
381 (zVAD-fmk) (ApexBio) as a pan-caspase inhibitor or 10 μM N-acetyl-tyrosyl-valyl-alanyl-
382 aspartyl chloromethyl ketone **(**Ac-YVAD-cmk, Calbiochem) as a caspase 1 inhibitor, 200 ng/mL
383 recombinant IL-1RA (Pepro Tech) or 50 ng/mL sTNFR1 (Pepro Tech) prior to challenge with *S.*
384 *pneumoniae*.

385

386 **Confocal immunofluorescence microscopy of mitochondria.**

387 To analyze mitochondrial network complexity mitochondrial outer membranes were stained and
388 analyzed by confocal microscopy as previously described (18). After the indicated time periods
389 macrophages were fixed with 4% paraformaldehyde for 20 min at room temperature (RT),
390 permeabilized using 0.1% Triton-X-100 with 50 mM NH_4Cl for 15 min, and blocked with
391 working solution PGAT (PGAT composition: 0.2% Gelatin with 0.02% Na-azide and 0.01%
392 Triton X-100 in PBS) for 15 min. The blocking solution was replaced with anti-translocase of
393 outer membrane 20 (TOMM20) (rabbit polyclonal IgG (FL-145) or mouse monoclonal IgG2a λ
394 (F10) when staining MDM, (both Santa Cruz) 200 μL/well at a 1:500 dilution in PGAT solution
395 and incubated overnight at $4^{o}C$. The following day, cells were washed 3 times with the PGAT

396 solution before being treated with secondary antibody Alexa Fluor 488-conjugated goat anti-
397 rabbit IgG (A11034; Thermo Fisher Scientific), Alexa Fluor 568-conjugated goat anti-rabbit IgG
398 (A11011; Thermo Fisher Scientific) or Alexa Fluor 488 conjugated goat polyclonal anti-mouse
399 IgG (A32723; Molecular Probes) at a 1:500 dilution in PGAT solution and incubated for 1 h at
400 RT. Cells were then washed three times in PGAT and twice in PBS. Nuclei were stained with 5
401 μM Draq5 (Biostatus Ltd. 1:1000 in PBS). Coverslips were mounted onto microscope slides with
402 a glycerol free poly-(vinyl alcohol) Tris-MWL 4-88 (Citifluor) mounting agent. To assess
403 mitochondrial network complexity, 8-12 Z-stack images per cell from 30 representative cells
404 after TOMM20 staining were acquired with a LSM510 inverted confocal fluorescence
405 microscope (Zeiss) using a 63x1.4 oil objective (zoom 2) lens, 488 nm and 633 nm excitations
406 lasers and 500-530 nm and 660-704 nm emission spectrums for TOMM20 and nuclear stains,
407 respectively. Z-stack images were converted into maximum projected images by ImageJ (v1.8,
408 NIH), as previously described (58). Subsequently, the single cell images were filtered using a 13
409 x 13 Mexican Hat shaped kernel, a filter defining the edges of the mitochondrial network (59),
410 before being subjected to a Huang threshold to remove background from the image (60). The
411 images were then skeletonized, removing any pixels touching a background pixel, except where
412 removal would result in the breaking of a continuous region of pixels, thus resulting in the
413 formation of a single pixel-wide skeleton. Finally, the binary connectivity was quantified using a
414 binary connectivity plugin (61) (plugins available from
415 http://www.mecourse.com/landinig/software/software.html and adapted by K. J. De Vos (18)) in
416 ImageJ software, as shown schematically in Fig. S1B and C. This plugin generates an output of 0
417 for background signal, 1 for a single pixel, 2 for an end point signal, 3 for a junction with two
418 neighboring pixels, 4 or more for a branch point with three or more neighboring pixels, as

419 described in the computational model developed by Sukhorukov et al. (62). The network
420 complexity of each individual cell was measured as the ratio of total branch points to total end
421 points. At least 300 representative macrophages were also counted per condition from the
422 acquired images and data recorded as the percentage of macrophages with fragmented
423 mitochondria. Macrophages were scored as having fragmented mitochondria if mitochondria
424 appeared fragmented. Macrophages were observed to show either a regular branched structure or
425 near complete loss of structure with virtually no cells showing partial degrees of fragmentation.
426 Filtered images are shown in Figures in the paper and the corresponding unfiltered images are
427 included in Fig. S7.

428 For mitochondrial co-staining with E3 ubiquitin ligase Parkin, BMDMs were labeled with rabbit
429 polyclonal anti-TOMM20 (Fl-145) and 1:500 mouse monoclonal anti-Parkin IgG2b κ (PRK8,
430 #32282 Santa Cruz) primary antibodies in PGAT solution overnight at 4°C and then Alexa Fluor
431 568 conjugated goat anti-rabbit and Alexa Fluor 488 conjugated goat anti-mouse secondary
432 antibodies. Nuclei were stained with Draq5 as above. Parkin fluorescence intensity for each
433 condition was measured as the corrected total cell fluorescence (CTCF) by ImageJ as described
434 (4). The Pearson's correlation coefficient for TOMM20 and Parkin in BMDMs was calculated as
435 described (4) .

436 To allow co-staining with LC3B, human MDM cultures (or positive-controls generated by
437 treatment with 20 μM carbonyl cyanide *p*-triflouromethoxy-phenylhydrazone (FCCP) for 12 h)
438 were labeled with mouse monoclonal anti-TOMM20 (F-10) and 1:500 rabbit polyclonal anti-
439 LC3B (ab48394, Abcam) primary antibodies, and subsequently Alexa Fluor 488 conjugated goat
440 anti-mouse and Alexa Fluor 568 conjugated goat polyclonal anti-rabbit secondary antibodies

441 (63). Nuclei were stained with Draq5.

442 For mitochondrial ROS (mROS) staining, cells with or without pre-treatment with MitoTempo
443 (Sigma-Aldrich) or CA-074me for 1 h before challenge with bacteria were washed 3 times with
444 pre-warmed Hanks' Balanced Salt Solution (HBSS, Thermo-Fisher Scientific) and mROS were
445 stained using 2.0 μM MitoSOX Red (Life Technologies) in pre-warmed phenol red free and
446 serum free RPMI media supplemented with 2 mM L-glutamine for 30 min. Cells were fixed with
447 2% paraformaldehyde (in PBS). Nuclei were stained with Draq5, coverslips mounted onto
448 microscope slides and Z-stack images were acquired, as above, using 488 nm and 633 nm
449 excitations lasers and 565-615 nm (for MitoSOX Red) and 661-704 nm (for Draq5) emission
450 spectrums. For quantification, mROS fluorescence intensity for each condition was measured as
451 the total corrected cell fluorescence, TCCF = integrated density – (area of selected cell - mean
452 fluorescence of control), as previously described (4). Unprocessed images were used for analysis
453 and depicted.

454 To measure apoptosis 200 μL/well NucView™ 530 red solution (2 μM in phenol red free and
455 serum free RMPI medium) (Biotium) was added for 30 min at 37°C and 5% CO_2. Cells were
456 fixed with 2% paraformaldehyde for 15 min at RT and DAPI (0.5 μg/mL in PBS) was added for
457 12 min at RT and cells were permeabilized and mitochondria stained as above. The NucView™
458 530 (red) positive DAPI (blue) positive cells were counted as apoptotic. At least 300 nuclei were
459 counted for each condition using the Zeiss LSM510 inverted fluorescence microscope.

460

461 **Transmission electron microscopy.**

462 Mouse BMDMs grown in T25 flasks were challenged with *S. pneumoniae* or mock-infected for
463 12 h then were washed 3 times with 2 ml Hanks' Balanced Salt Solution (HBSS) per flask and
464 accutase was added for 15 min at 37°C and 5% CO_2. The cell suspension was centrifuged at
465 2000g for 10 min, washed once with HBSS and centrifuged again at 2000g for 10 min. The
466 pellet was fixed overnight with 2.5% glutaraldehyde in 0.1 M sodium phosphate buffer at 4°C.
467 The pellet was then washed twice with 0.1 M sodium cacodylate buffer for 30 min at 4°C.
468 Secondary fixation was carried out in 2% aqueous osmium tetroxide for 2 h at room temperature
469 (RT) as previously described (68), then washed free from secondary fixative twice with 0.1 M
470 sodium cacodylate buffer for 30 min before being dehydrated through a graded series of ethanol
471 solutions in water; 75%, 95%, and 100%, and 100% ethanol dried over anhydrous copper
472 sulphate for 15 min each at RT. The pellet was cleared of ethanol in an intermediate solvent of
473 propylene oxide for 15 min, twice, at RT, before being infiltrated by in a 50/50 mixture of
474 propylene oxide/araldite resin overnight at RT on a rotor mixer in a fume hood. The following
475 day this mixture was mostly discarded, the remainder propylene oxide evaporated in the fume
476 hood leaving the pellet which was then placed in full strength araldite resin with one change, for
477 6-8 h at RT.
478 Subsequently the specimen pellet was embedded in fresh araldite resin and cured at 60°C for 48-
479 72 hrs. Ultrathin (~85 nm) sections were cut on a Reichert Ultracut E ultramicrotome with a
480 diamond knife, transferred to copper grids and stained with uranyl acetate and lead citrate.
481 Electron micrographs were recorded at 80 kV at a nominal magnification of 13,000x on a FEI
482 Tecnai G2 Biotwin Spirit microscope equipped with a Gatan Orius digital camera. The mean
483 number of cristae per mitochondria for 13-62 mitochondria was recorded for each condition.
484

485 **Metabolic measurements.**

486 Macrophages grown in T75 flasks for 14 d were washed once with sterile Dulbecco's PBS (Life
487 Technologies) and treated with accutase (Biolegend) for 15 min at 37°C and 5% CO_2. The
488 detached cells were re-seeded in XF24 cell plates (Agilent Technologies) at 150,000 MDMs/well
489 or 200,000 BMDMs/well. Cultures were then challenged with bacteria or mock-infected in the
490 presence or absence of MitoTempo and at the indicated time points cultures were washed twice
491 with XF medium supplemented with 4.5 g/L D-glucose, 2.0 mM L-glutamine, 1.0 mM sodium-
492 pyruvate, 100 U/L penicillin and 100 µg/mL streptomycin at pH 7.4 (adjusted with 1.0 M
493 NaOH). Next 630 µL modified XF medium was added to each well and incubated for 1 h at
494 37°C without CO_2. At the same time the XF24 utility plate, containing sensors probes, was set
495 up using a plate previously submerged and incubated in XF calibrant (Agilent Technologies)
496 overnight at 37°C. 70 µL oligomycin A (15 µM), 77 µL FCCP (20 µM) and 85 µL rotenone (10
497 µM) plus antimycin A (10 µM) (all Sigma-Aldrich) were added to the cartridge injection ports A,
498 B and C, respectively and incubated for 1 h at 37°C without CO_2. Finally, the calibration plate
499 was loaded into the XF24 flux analyser. After calibration completion, the utility plate without
500 cartridge was unloaded and the cell plate was loaded into the XF24 analyser (Seahorse, Agilent
501 Technologies). After equilibration, the cartridge containing the oxygen sensor, measuring the
502 oxygen consumption rate (OCR) and the cartridge containing the proton sensor, measuring the
503 extracellular acidification rate (ECAR) kinetics were run before and after injecting oligomycin,
504 FCCP and rotenone plus antimycin A, respectively. The key parameters of mitochondrial
505 oxidative phosphorylation and cytosolic glycolysis were calculated from OCR and ECAR,
506 respectively, as described in (64). The ATP synthase inhibitor oligomycin A (oligo) was added
507 after baseline OCR acquisition, to measure ATP-linked OCR. The maximum respiration capacity

508 was measured by subtracting non-mitochondrial OCR [calculated following treatment with
509 rotenone (Rot) plus antimycin A (AntA)] from Carbonyl cyanide 4-(trifluoromethoxy)
510 phenylhydrazone (FCCP) treated OCR. Data were normalized by total protein.

511

512 **Flow cytometry.**

513 Mitochondrial specific ROS was also measured by flow cytometry. Macrophages were stained
514 using 2.0 μM MitoSOX Red (Life Technologies) diluted in pre-warmed phenol red free RPMI
515 media supplemented with 2mM L- glutamine and incubated for 30 min at 37°C and 5% CO_2. As
516 a positive control, BMDM were treated with rotenone (2.0 μM) and antimycin A (10 μM) for 30
517 min at 37°C and 5% CO_2. Loss of mitochondrial inner transmembrane potential ($\Delta\psi_m$) was
518 measured with 10 μM of 5,5′,6,6′-tetrachloro-1,1′,3,3′-tetraethyl benzimidazolyl carbocyanine
519 iodide (JC-1; eBioscience), diluted in phenol red free RPMI media supplemented with 2 mM L-
520 glutamine) (eBioscience, 65-0851-38) for 30 min at 37°C with 5% CO_2. Cells were re-
521 suspended in PBS (300 μL/well), after gentle scrapping and washing 3 times with HBSS. Both
522 oxidized MitoSOX Red and the loss of JC-1 aggregates as a marker of loss of $\Delta\psi_m$ were
523 measured using a FACS Calibur (Becton Dickinson) via the FL-2H channel. The forward and
524 side scatters were used to distinguish cell populations and a total of 10,000 events were recorded.
525 The instrument settings were saved and used for subsequent sample acquisition and analyses.
526 Data were analyzed using FlowJo software, version 8.8.4 (Tree Star Inc.).

527

528 **Cytokine assay.**

529 IL-1β and TNF-α levels in the culture supernatants were measured using mouse IL-1β and TNF-
530 α DuoSet enzyme-linked immunosorbent assay (ELISA) kits, respectively (eBioscience,
531 Hatfield, United Kingdom) according to the manufacturer's specifications.

532

533 **Intracellular killing assay.**

534 The intracellular killing assays were carried out as previously described (8). To perform
535 modified gentamicin protection assays cells were treated at the indicated time points with 20
536 μg/mL gentamicin and 40 U/mL penicillin G (Sigma, PENNA-100MU) for 30 min at 37°C and
537 5% CO_2, to kill extracellular bacteria. Subsequently cells were washed 3 times with PBS before
538 being treated with 2% saponin (250 μL/well) (Sigma) in distilled water and incubated for 15 min
539 at 37°C and 5% CO2. In some experiments 12 h and 16 h killing assays, macrophages were
540 performed in the presence or absence of the indicated inhibitors or vehicle controls. In these
541 experiments the appropriate reagent was added 1 h before bacterial challenge, added again at the
542 time of bacterial challenge and at the 4 h time point after bacteria were washed off. For 16h
543 killing assays, macrophages were 'pulsed' with gentamicin and penicillin G at 12 h as above,
544 then 'chased' with 0.75μg/mL vancomycin (Sigma) in the presence of the appropriate reagent for
545 a further 4 h before washing and saponin lysis (8).To perform surface viable counts, 750 μL PBS
546 was added to each well and macrophages were lysed with vigorous pipetting and scraping across
547 the wells. Subsequently the lysates were serially diluted and plated on Columbia blood agar
548 plates. Data were calculated as cfu/mL and ratios of inhibitors compared to vehicle controls.

549

550 **SDS-PAGE and Western blotting.**

551 Macrophages cultured in T25 flasks were challenged with bacteria or mock-infected and
552 cytosolic or mitochondrial fractions isolated as described previously (65). Protein was quantified
553 using a modified Lowry protocol (*DC* protein assay; Bio-Rad Laboratories), and equal protein
554 was loaded per lane, 20 μg of protein from cytosolic and 10 μg from mitochondrial fractions.
555 Samples were separated by SDS-PAGE (12%) and blotted onto poly-vinylidene difluoride
556 (PVDF) membranes (Bio-Rad Laboratories) with protein transfer confirmed by Ponceau S
557 staining. Blots were incubated overnight at 4°C with antibodies against Parkin (PARK8, mouse
558 monoclonal, Santa-Cruz Biotechnology Inc., cat no. SC-32282, 1:200 dilution in 5% milk TBS-
559 tween), Actin (Rabbit polyclonal, Sigma-Aldrich 1:10000 dilution) or Voltage dependent anion
560 channel (VDAC) (Rabbit polyclonal, Cell Signaling Tech. lot-4, 1:1000 dilution). Protein
561 detection was carried out with horseradish peroxidase (HRP)-conjugated secondary antibodies,
562 goat anti–mouse (Dako, P0447, 1:2500 dilution) or goat anti-rabbit IgG (Dako, P0448, 1:2500)
563 and ECL substrate (GE Healthcare). Bands were quantified using Image J 1.32 software (v1.8,
564 NIH). The intensity ratio of Parkin and actin, and Parkin and VDAC were calculated.

565 **Statistics**

566 Data are represented as mean and standard error of the mean unless otherwise indicated in the
567 Figure legends. Statistical significance was determined using ANOVA with Sidak's or
568 Bonferroni's post-hoc multiple comparisons test and pair-wise comparisons were done with
569 student paired t-test. Analysis was performed using Prism 7.0 software (GraphPad Inc.) and
570 significance defined as $p < 0.05$.
571

572 **ACKNOWLEDGMENTS**

573 The authors' work is supported by a Commonwealth studentship award funded by the UK
574 government to MM (CSBD-2014-52., by the MRC SHIELD consortium (DHD PI)),
575 MRNO2995X/1 and by an Innovation grant from the Antimicrobial Resistance Cross Council
576 Initiative supported by the seven research councils (MR/M017931/1) to HMM. Electron
577 microscopy support was provided through the University of Sheffield's Faculty of Science
578 Electron Microscopy Facility. PJS is supported as an NIHR Senior Investigator and by the NIHR
579 Sheffield Biomedical Research Centre. Confocal microscopy support in Edinburgh was provided
580 by the Queen's Medical Research Institute Confocal and Advanced Light Microscopy Facility
581 (QMRI CALM), and flow cytometry support in Edinburgh was provided by the QMRI Flow
582 Cytometry and Cell Sorting Facility at the University of Edinburgh.

583

584 **AUTHOR CONTRIBUTIONS**

585 MM, KBC, EF, ECP, CDR and JM conducted and analysed experiments. SPA and PJS provided
586 expertise and access to equipment to facilitate Seahorse experiments. CP provided tissue culture
587 and macrophage characterization expertise. KJdV provided expertise and methodology to enable
588 imaging based analysis of fission. CJH and PB provided expertise in electron microscopy. AMC
589 provided reagents and shared expertise in analysis of PI3K pathways. TJM provided expertise in
590 microbiology and generated mutants used in experiments. HMM and DHD designed experiments
591 and reviewed analysis with MM and KBC. MM, KBC, HMM, DHD wrote the paper with input
592 from all authors.

593

COMPETING INTERESTS

The authors declare no competing interests.

597 **REFERENCES**

598 1. Dockrell DH, Marriott HM, Prince LR, Ridger VC, Ince PG, Hellewell PG, Whyte MK.
599 2003. Alveolar macrophage apoptosis contributes to pneumococcal clearance in a
600 resolving model of pulmonary infection. J Immunol 171:5380-8.
601 2. Cole J, Aberdein J, Jubrail J, Dockrell DH. 2014. The role of macrophages in the innate
602 immune response to Streptococcus pneumoniae and Staphylococcus aureus: mechanisms
603 and contrasts. Adv Microb Physiol 65:125-202.
604 3. Dockrell DH, Whyte MKB, Mitchell TJ. 2012. Pneumococcal pneumonia: mechanisms
605 of infection and resolution. Chest 142:482-491.
606 4. Bewley MA, Preston JA, Mohasin M, Marriott HM, Budd RC, Swales J, Collini P,
607 Greaves DR, Craig RW, Brightling CE, Donnelly LE, Barnes PJ, Singh D, Shapiro SD,
608 Whyte MKB, Dockrell DH. 2017. Impaired Mitochondrial Microbicidal Responses in
609 Chronic Obstructive Pulmonary Disease Macrophages. Am J Respir Crit Care Med
610 196:845-855.
611 5. Weinberg SE, Sena LA, Chandel NS. 2015. Mitochondria in the regulation of innate and
612 adaptive immunity. Immunity 42:406-17.
613 6. Sancho D, Enamorado M, Garaude J. 2017. Innate Immune Function of Mitochondrial
614 Metabolism. Front Immunol 8:527.
615 7. West AP, Brodsky IE, Rahner C, Woo DK, Erdjument-Bromage H, Tempst P, Walsh
616 MC, Choi Y, Shadel GS, Ghosh S. 2011. TLR signalling augments macrophage
617 bactericidal activity through mitochondrial ROS. Nature 472:476-80.
618 8. Preston JA, Bewley MA, Marriott HM, Houghton AM, Mohasin M, Jubrail J, Morris L,
619 Stephenson YL, Cross S, Greaves DR, Craig RW, van Rooijen N, Bingle CD, Read RC,

620 Mitchell TJ, Whyte MKB, Shapiro SD, Dockrell DH. 2019. Alveolar Macrophage
621 Apoptosis-Associated Bacterial Killing Helps Prevent Murine Pneumonia. Am J Respir
622 Crit Care Med 200:84-97.
623 9. O'Neill LA, Kishton RJ, Rathmell J. 2016. A guide to immunometabolism for
624 immunologists. Nat Rev Immunol 16:553-65.
625 10. Youle RJ, van der Bliek AM. 2012. Mitochondrial fission, fusion, and stress. Science
626 337:1062-5.
627 11. Rossignol R, Gilkerson R, Aggeler R, Yamagata K, Remington SJ, Capaldi RA. 2004.
628 Energy substrate modulates mitochondrial structure and oxidative capacity in cancer
629 cells. Cancer Res 64:985-93.
630 12. Yu T, Robotham JL, Yoon Y. 2006. Increased production of reactive oxygen species in
631 hyperglycemic conditions requires dynamic change of mitochondrial morphology. Proc
632 Natl Acad Sci U S A 103:2653-8.
633 13. Biswas SK, Mantovani A. 2012. Orchestration of metabolism by macrophages. Cell
634 Metab 15:432-7.
635 14. O'Neill LA, Pearce EJ. 2016. Immunometabolism governs dendritic cell and macrophage
636 function. J Exp Med 213:15-23.
637 15. Kelly B, O'Neill LA. 2015. Metabolic reprogramming in macrophages and dendritic cells
638 in innate immunity. Cell Res 25:771-84.
639 16. Mohammed Mohasin KB-C, Emily Fisk, Elizabeth C. Prestwich, Clark D. Russell,
640 Jennifer Marshall, Clare Pridans, Scott P. Allen, Pamela J. Shaw, Kurt J. De Vos,
641 Christopher J. Hill, Per Bullough, Alison M. Condliffe, Tim J. Mitchell, Helen M.
642 Marriott, David H. Dockrell. 2019. Macrophages utilize mitochondrial fission to enhance

643 mROS production during responses to *Streptococcus pneumoniae*. bioRxiv
644 doi:https://doi.org/10.1101/722603.
645 17. Daigneault M, Preston JA, Marriott HM, Whyte MK, Dockrell DH. 2010. The
646 identification of markers of macrophage differentiation in PMA-stimulated THP-1 cells
647 and monocyte-derived macrophages. PLoS One 5:e8668.
648 18. De Vos KJ, Sheetz MP. 2007. Visualization and quantification of mitochondrial
649 dynamics in living animal cells. Methods Cell Biol 80:627-82.
650 19. Stavru F, Palmer AE, Wang C, Youle RJ, Cossart P. 2013. Atypical mitochondrial fission
651 upon bacterial infection. Proc Natl Acad Sci U S A 110:16003-8.
652 20. Stavru F, Bouillaud F, Sartori A, Ricquier D, Cossart P. 2011. Listeria monocytogenes
653 transiently alters mitochondrial dynamics during infection. Proc Natl Acad Sci U S A
654 108:3612-7.
655 21. Bewley MA, Naughton M, Preston J, Mitchell A, Holmes A, Marriott HM, Read RC,
656 Mitchell TJ, Whyte MK, Dockrell DH. 2014. Pneumolysin activates macrophage
657 lysosomal membrane permeabilization and executes apoptosis by distinct mechanisms
658 without membrane pore formation. MBio 5:e01710-14.
659 22. Mishra P, Chan DC. 2016. Metabolic regulation of mitochondrial dynamics. J Cell Biol
660 212:379-87.
661 23. Jastroch M, Divakaruni AS, Mookerjee S, Treberg JR, Brand MD. 2010. Mitochondrial
662 proton and electron leaks. Essays Biochem 47:53-67.
663 24. Peterman EM, Sullivan C, Goody MF, Rodriguez-Nunez I, Yoder JA, Kim CH. 2015.
664 Neutralization of mitochondrial superoxide by superoxide dismutase 2 promotes bacterial
665 clearance and regulates phagocyte numbers in zebrafish. Infect Immun 83:430-40.

666 25. Bauerfeld CP, Rastogi R, Pirockinaite G, Lee I, Huttemann M, Monks B, Birnbaum MJ,
667 Franchi L, Nunez G, Samavati L. 2012. TLR4-mediated AKT activation is MyD88/TRIF
668 dependent and critical for induction of oxidative phosphorylation and mitochondrial
669 transcription factor A in murine macrophages. J Immunol 188:2847-57.
670 26. Akira S, Takeda K. 2004. Toll-like receptor signalling. Nat Rev Immunol 4:499-511.
671 27. Costa C, Martin-Conte EL, Hirsch E. 2011. Phosphoinositide 3-kinase p110gamma in
672 immunity. IUBMB Life 63:707-13.
673 28. Heid ME, Keyel PA, Kamga C, Shiva S, Watkins SC, Salter RD. 2013. Mitochondrial
674 reactive oxygen species induces NLRP3-dependent lysosomal damage and
675 inflammasome activation. J Immunol 191:5230-8.
676 29. Zhao M, Antunes F, Eaton JW, Brunk UT. 2003. Lysosomal enzymes promote
677 mitochondrial oxidant production, cytochrome c release and apoptosis. Eur J Biochem
678 270:3778-86.
679 30. Abuarab N, Munsey TS, Jiang LH, Li J, Sivaprasadarao A. 2017. High glucose-induced
680 ROS activates TRPM2 to trigger lysosomal membrane permeabilization and Zn(2+)-
681 mediated mitochondrial fission. Sci Signal 10.
682 31. Chu J, Thomas LM, Watkins SC, Franchi L, Nunez G, Salter RD. 2009. Cholesterol-
683 dependent cytolysins induce rapid release of mature IL-1beta from murine macrophages
684 in a NLRP3 inflammasome and cathepsin B-dependent manner. J Leukoc Biol 86:1227-
685 38.
686 32. Marriott HM, Bingle CD, Read RC, Braley KE, Kroemer G, Hellewell PG, Craig RW,
687 Whyte MK, Dockrell DH. 2005. Dynamic changes in Mcl-1 expression regulate

688 macrophage viability or commitment to apoptosis during bacterial clearance. J Clin
689 Invest 115:359-68.
690 33. Tannahill GM, Curtis AM, Adamik J, Palsson-McDermott EM, McGettrick AF, Goel G,
691 Frezza C, Bernard NJ, Kelly B, Foley NH, Zheng L, Gardet A, Tong Z, Jany SS, Corr
692 SC, Haneklaus M, Caffrey BE, Pierce K, Walmsley S, Beasley FC, Cummins E, Nizet V,
693 Whyte M, Taylor CT, Lin H, Masters SL, Gottlieb E, Kelly VP, Clish C, Auron PE,
694 Xavier RJ, O'Neill LA. 2013. Succinate is an inflammatory signal that induces IL-1beta
695 through HIF-1alpha. Nature 496:238-42.
696 34. Zhou R, Yazdi AS, Menu P, Tschopp J. 2011. A role for mitochondria in NLRP3
697 inflammasome activation. Nature 469:221-5.
698 35. Garaude J, Acin-Perez R, Martinez-Cano S, Enamorado M, Ugolini M, Nistal-Villan E,
699 Hervas-Stubbs S, Pelegrin P, Sander LE, Enriquez JA, Sancho D. 2016. Mitochondrial
700 respiratory-chain adaptations in macrophages contribute to antibacterial host defense. Nat
701 Immunol 17:1037-1045.
702 36. Buck MD, O'Sullivan D, Klein Geltink RI, Curtis JD, Chang CH, Sanin DE, Qiu J, Kretz
703 O, Braas D, van der Windt GJ, Chen Q, Huang SC, O'Neill CM, Edelson BT, Pearce EJ,
704 Sesaki H, Huber TB, Rambold AS, Pearce EL. 2016. Mitochondrial Dynamics Controls
705 T Cell Fate through Metabolic Programming. Cell 166:63-76.
706 37. Bordt EA, Clerc P, Roelofs BA, Saladino AJ, Tretter L, Adam-Vizi V, Cherok E, Khalil
707 A, Yadava N, Ge SX, Francis TC, Kennedy NW, Picton LK, Kumar T, Uppuluri S,
708 Miller AM, Itoh K, Karbowski M, Sesaki H, Hill RB, Polster BM. 2017. The Putative
709 Drp1 Inhibitor mdivi-1 Is a Reversible Mitochondrial Complex I Inhibitor that Modulates
710 Reactive Oxygen Species. Dev Cell 40:583-594 e6.

711 38. Rambold AS, Pearce EL. 2018. Mitochondrial Dynamics at the Interface of Immune Cell
712 Metabolism and Function. Trends Immunol 39:6-18.
713 39. Rayamajhi M, Miao EA. 2014. The RIP1-RIP3 complex initiates mitochondrial fission to
714 fuel NLRP3. Nat Immunol 15:1100-2.
715 40. Wang X, Jiang W, Yan Y, Gong T, Han J, Tian Z, Zhou R. 2014. RNA viruses promote
716 activation of the NLRP3 inflammasome through a RIP1-RIP3-DRP1 signaling pathway.
717 Nat Immunol 15:1126-33.
718 41. Ichinohe T, Yamazaki T, Koshiba T, Yanagi Y. 2013. Mitochondrial protein mitofusin 2
719 is required for NLRP3 inflammasome activation after RNA virus infection. Proc Natl
720 Acad Sci U S A 110:17963-8.
721 42. Park S, Won JH, Hwang I, Hong S, Lee HK, Yu JW. 2015. Defective mitochondrial
722 fission augments NLRP3 inflammasome activation. Sci Rep 5:15489.
723 43. Hawkins PT, Stephens LR. 2015. PI3K signalling in inflammation. Biochim Biophys
724 Acta 1851:882-97.
725 44. Caino MC, Ghosh JC, Chae YC, Vaira V, Rivadeneira DB, Faversani A, Rampini P,
726 Kossenkov AV, Aird KM, Zhang R, Webster MR, Weeraratna AT, Bosari S, Languino
727 LR, Altieri DC. 2015. PI3K therapy reprograms mitochondrial trafficking to fuel tumor
728 cell invasion. Proc Natl Acad Sci U S A 112:8638-43.
729 45. Weber K, Schilling JD. 2014. Lysosomes integrate metabolic-inflammatory cross-talk in
730 primary macrophage inflammasome activation. J Biol Chem 289:9158-71.
731 46. He Y, Hara H, Nunez G. 2016. Mechanism and Regulation of NLRP3 Inflammasome
732 Activation. Trends Biochem Sci 41:1012-1021.

733 47. McLelland GL, Soubannier V, Chen CX, McBride HM, Fon EA. 2014. Parkin and
734 PINK1 function in a vesicular trafficking pathway regulating mitochondrial quality
735 control. EMBO J 33:282-95.
736 48. Twig G, Elorza A, Molina AJ, Mohamed H, Wikstrom JD, Walzer G, Stiles L, Haigh SE,
737 Katz S, Las G, Alroy J, Wu M, Py BF, Yuan J, Deeney JT, Corkey BE, Shirihai OS.
738 2008. Fission and selective fusion govern mitochondrial segregation and elimination by
739 autophagy. EMBO J 27:433-46.
740 49. Montessuit S, Somasekharan SP, Terrones O, Lucken-Ardjomande S, Herzig S,
741 Schwarzenbacher R, Manstein DJ, Bossy-Wetzel E, Basanez G, Meda P, Martinou JC.
742 2010. Membrane remodeling induced by the dynamin-related protein Drp1 stimulates
743 Bax oligomerization. Cell 142:889-901.
744 50. Suen DF, Norris KL, Youle RJ. 2008. Mitochondrial dynamics and apoptosis. Genes Dev
745 22:1577-90.
746 51. Narendra D, Tanaka A, Suen DF, Youle RJ. 2008. Parkin is recruited selectively to
747 impaired mitochondria and promotes their autophagy. J Cell Biol 183:795-803.
748 52. Carroll RG, Hollville E, Martin SJ. 2014. Parkin sensitizes toward apoptosis induced by
749 mitochondrial depolarization through promoting degradation of Mcl-1. Cell Rep 9:1538-
750 53.
751 53. Bewley MA, Marriott HM, Tulone C, Francis SE, Mitchell TJ, Read RC, Chain B,
752 Kroemer G, Whyte MK, Dockrell DH. 2011. A cardinal role for cathepsin d in co-
753 ordinating the host-mediated apoptosis of macrophages and killing of pneumococci.
754 PLoS Pathog 7:e1001262.

755 54. Chan DC. 2006. Mitochondria: dynamic organelles in disease, aging, and development.
756 Cell 125:1241-52.
757 55. Frank S, Gaume B, Bergmann-Leitner ES, Leitner WW, Robert EG, Catez F, Smith CL,
758 Youle RJ. 2001. The role of dynamin-related protein 1, a mediator of mitochondrial
759 fission, in apoptosis. Dev Cell 1:515-25.
760 56. Aberdein JD, Cole J, Bewley MA, Marriott HM, Dockrell DH. 2013. Alveolar
761 macrophages in pulmonary host defence the unrecognized role of apoptosis as a
762 mechanism of intracellular bacterial killing. Clin Exp Immunol 174:193-202.
763 57. Dockrell DH, Lee M, Lynch DH, Read RC. 2001. Immune-mediated phagocytosis and
764 killing of Streptococcus pneumoniae are associated with direct and bystander
765 macrophage apoptosis. J Infect Dis 184:713-22.
766 58. Nikolaisen J, Nilsson LI, Pettersen IK, Willems PH, Lorens JB, Koopman WJ, Tronstad
767 KJ. 2014. Automated quantification and integrative analysis of 2D and 3D mitochondrial
768 shape and network properties. PLoS One 9:e101365.
769 59. Koopman WJ, Visch HJ, Verkaart S, van den Heuvel LW, Smeitink JA, Willems PH.
770 2005. Mitochondrial network complexity and pathological decrease in complex I activity
771 are tightly correlated in isolated human complex I deficiency. Am J Physiol Cell Physiol
772 289:C881-90.
773 60. Huang L-KaW, M-J. 1995. Image Thresholding by Minimizing the Measures of
774 Fuzziness. Pattern Recognition 28:41-51.
775 61. Landini G. 2008. Advanced shape analysis with ImageJ. , p 116-121. *In* (ed), Proceedings
776 of the Second ImageJ User and Developer Conference, Luxembourg.

777 62. Sukhorukov VM, Dikov D, Reichert AS, Meyer-Hermann M. 2012. Emergence of the
778 mitochondrial reticulum from fission and fusion dynamics. PLoS Comput Biol
779 8:e1002745.
780 63. Costello MJ, Brennan LA, Basu S, Chauss D, Mohamed A, Gilliland KO, Johnsen S,
781 Menko S, Kantorow M. 2013. Autophagy and mitophagy participate in ocular lens
782 organelle degradation. Exp Eye Res 116:141-50.
783 64. Pelletier M, Billingham LK, Ramaswamy M, Siegel RM. 2014. Extracellular flux
784 analysis to monitor glycolytic rates and mitochondrial oxygen consumption. Methods
785 Enzymol 542:125-49.
786 65. Marriott HM, Ali F, Read RC, Mitchell TJ, Whyte MK, Dockrell DH. 2004. Nitric oxide
787 levels regulate macrophage commitment to apoptosis or necrosis during pneumococcal
788 infection. FASEB J 18:1126-8.
789

790

791 **FIGURES**

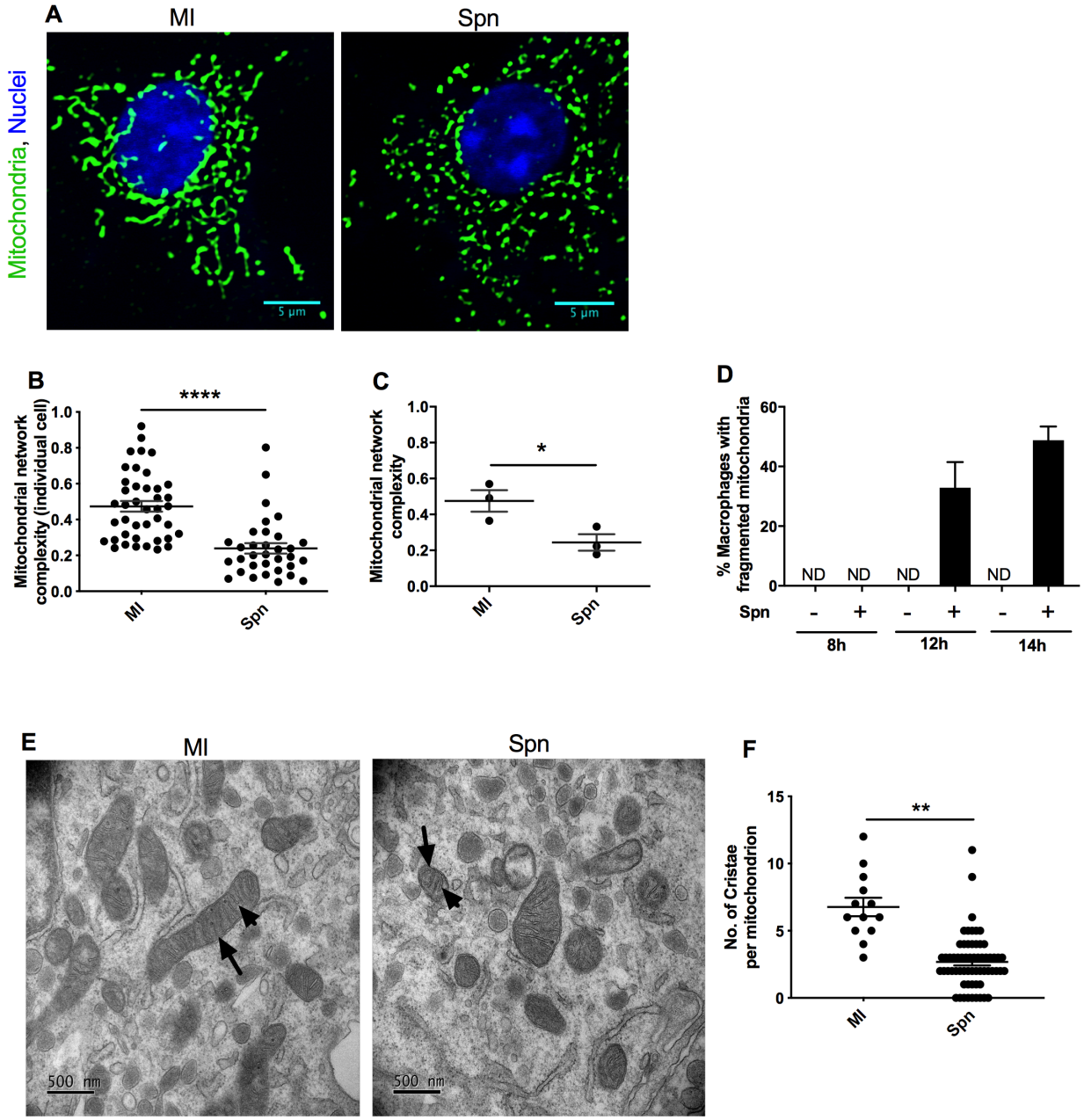

792

793 **Fig 1. Sustained exposure to *S. pneumoniae* results in increased mitochondrial**

794 **fragmentation.** Bone marrow derived macrophages (BMDMs) were mock-infected (MI) or

795 exposed to *S. pneumoniae* (Spn) at a MOI of 10, for 8-14 h. (A-D) Confocal microscopy was

796 performed after staining with the mitochondrial outer membrane specific marker TOMM20

797 (green) to delineate mitochondrial structure. (A) Representative filtered images of mitochondrial
798 structure in BMDMs 12 h after exposure under each experimental condition, scale bars = 5 μm,
799 from one of three independent experiments; (B) calculated mitochondrial network complexity
800 (n≥30 cells per condition) across the three independent experiments at 12 h; (C) average
801 calculated mitochondrial network complexity under each condition in the three independent
802 experiments at 12 h; (D) percentage of macrophages with fragmented mitochondria at 8, 12 and
803 14 h post-bacterial challenge (Spn+) or MI (Spn-), calculated from three independent
804 experiments. (E-F) MI or Spn BMDMs 12 h after challenge were also imaged by transmission
805 electron microscopy. (E) Representative electron micrographs, from one of three independent
806 experiments are shown, scale bars = 500nm. Arrows show mitochondria and arrowheads show
807 cristae; (F) number of cristae per mitochondrion in representative slices were calculated (MI,
808 n=13, Spn, n=62). Data are shown as mean ± SEM. Statistical analysis was performed with one-
809 way ANOVA and Bonferroni post-hoc test (B-C), student paired *t* test (F). *$p<0.05$, ** $p<0.01$,
810 ****$p<0.0001$. ND=not detected.

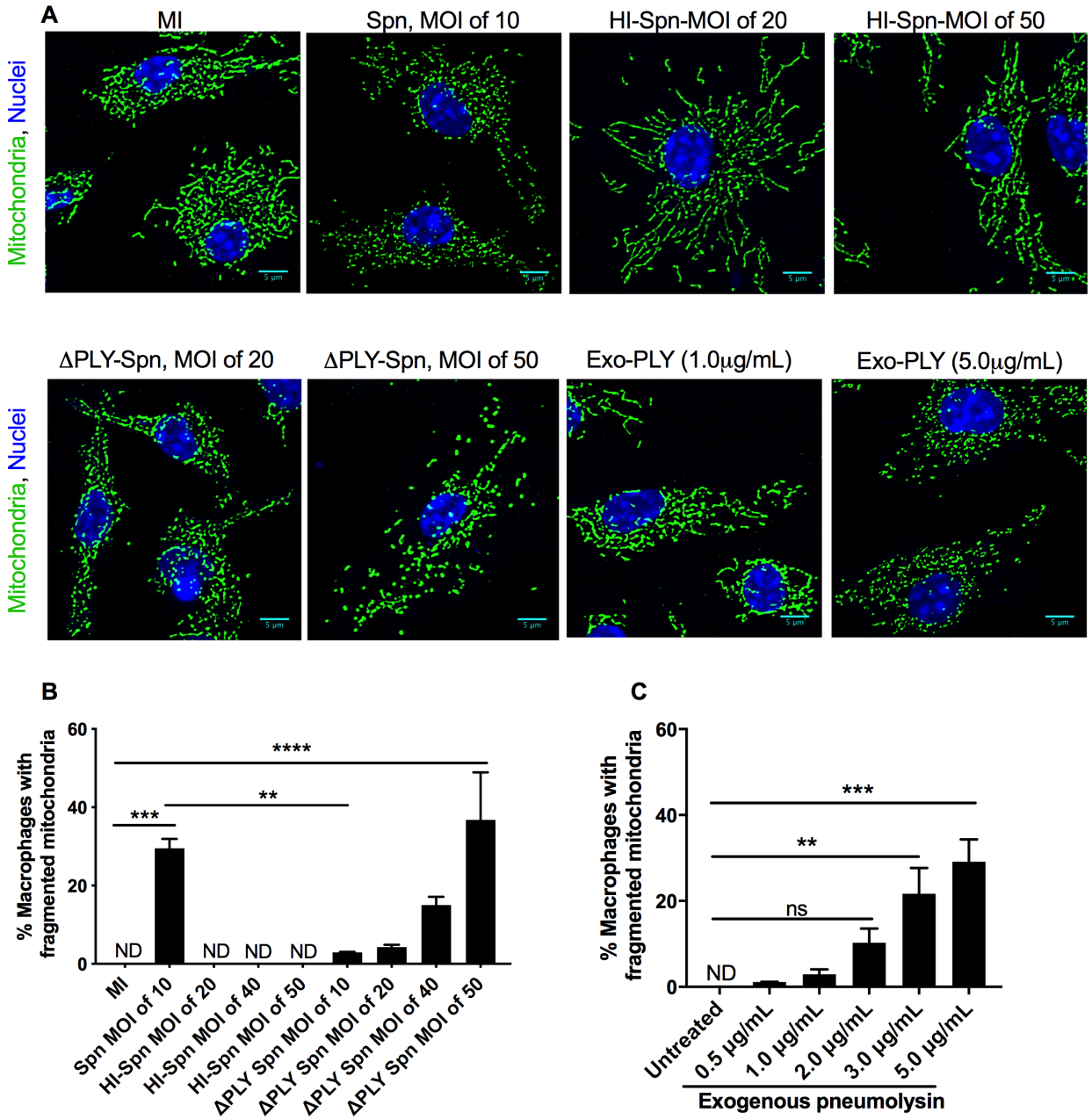

Fig 2. The pore-forming toxin pneumolysin is not essential to trigger increased mitochondrial fission. BMDMs were mock-infected (MI), challenged with *S. pneumoniae* (Spn), heat inactivated Spn (HI-Spn) or a pneumolysin deficient Spn mutant (ΔPLY Spn), at the indicated multiplicity of infection, or alternatively with exogenous pneumolysin (0.5 μg/mL-5 μg/mL) for 12 h. Confocal microscopy was performed after staining with the mitochondrial outer

817 membrane specific marker TOMM20 (green) to delineate mitochondrial structure or with Draq5
818 to label nuclei (blue). (A) Representative filtered images of mitochondrial structure in BMDMs
819 under a range of conditions, scale bars = 5 μm, from one of three independent experiments.
820 Percentage of macrophages with fragmented mitochondria after challenge with (B) each strain of
821 bacteria or (C) each concentration of pneumolysin. Data are shown as mean ± SEM, (n=3).
822 Statistical analysis was performed with one-way ANOVA and Sidak's multiple comparison (B)
823 or Bonferroni post-hoc test (C), * $p<0.05$, ** $p<0.01$, ****$p<0.0001$. ND=not detected.

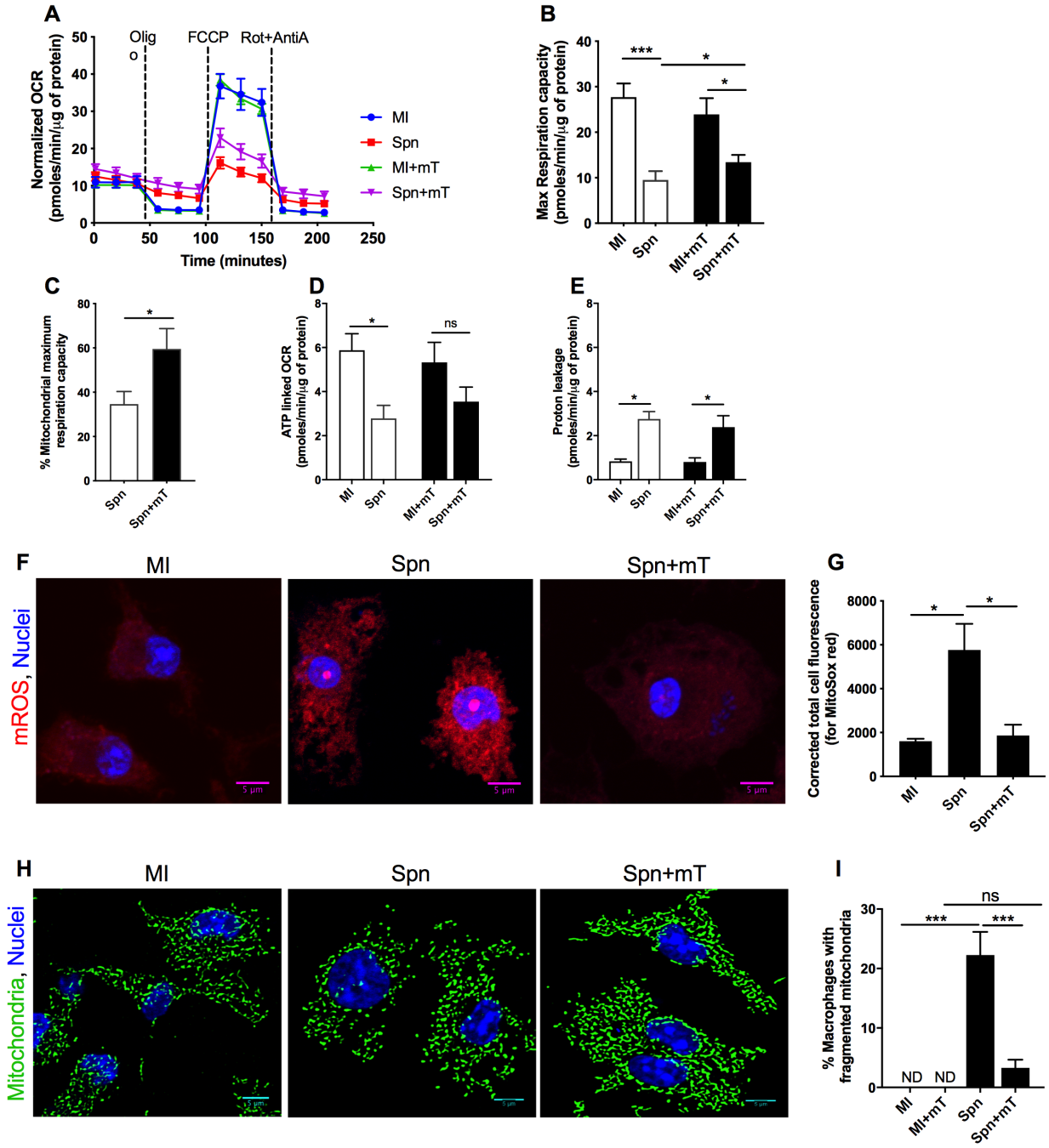

Fig 3. mROS contributes to increased mitochondrial fission and metabolic adaption following bacterial challenge. BMDMs were mock-infected (MI) or challenged with *S. pneumoniae* (Spn) for 12 h after pre-treatment with the mROS inhibitor MitoTempo (+mT) or vehicle control. Subsequently, the mitochondrial oxygen consumption rate (OCR) was measured

829 by the Seahorse X24 extracellular flux analyser. The ATP synthase inhibitor oligomycin A
830 (oligo) was added after baseline OCR acquisition, to measure ATP-linked OCR. The maximum
831 respiration capacity was measured by subtracting non-mitochondrial OCR [calculated following
832 treatment with rotenone (Rot) plus antimycin A (AntA)] from Carbonyl cyanide 4-
833 (trifluoromethoxy) phenylhydrazone (FCCP) treated OCR. (A) Representative graph of the OCR
834 kinetic data with each condition from one experiment. From the OCR kinetic data, the
835 mitochondrial maximum respiration capacity (MRC) (B), percentage of mitochondrial MRC
836 after bacterial challenge with or without mT (C), ATP-linked OCR (D) and proton leakage (E)
837 were calculated. (A-E), n=4. (F-G) Under the same conditions BMDMs were stained with
838 MitoSOX Red to detect mROS (red) or nuclei stained with Draq5 (blue) and imaged by confocal
839 microscopy. (F) Representative unprocessed images from one of three independent experiments
840 are shown and (G) corrected total cell fluorescence was calculated, (n=3). (H-I) Under the same
841 conditions mitochondria were stained with anti-TOMM20 (green) and examined by confocal
842 microscopy. (H) Representative filtered images from three independent experiments are shown
843 and (I) the percentage of macrophages with fragmented mitochondria was calculated, (n=300).
844 Data are shown as mean ± SEM. Statistical analysis was performed with one-way ANOVA with
845 Sidak's post-hoc test for multiple comparisons and student paired *t* test for pair-wise comparison
846 in (C). *$p \leq 0.05$, ***$p \leq 0.001$. ND=not detected.

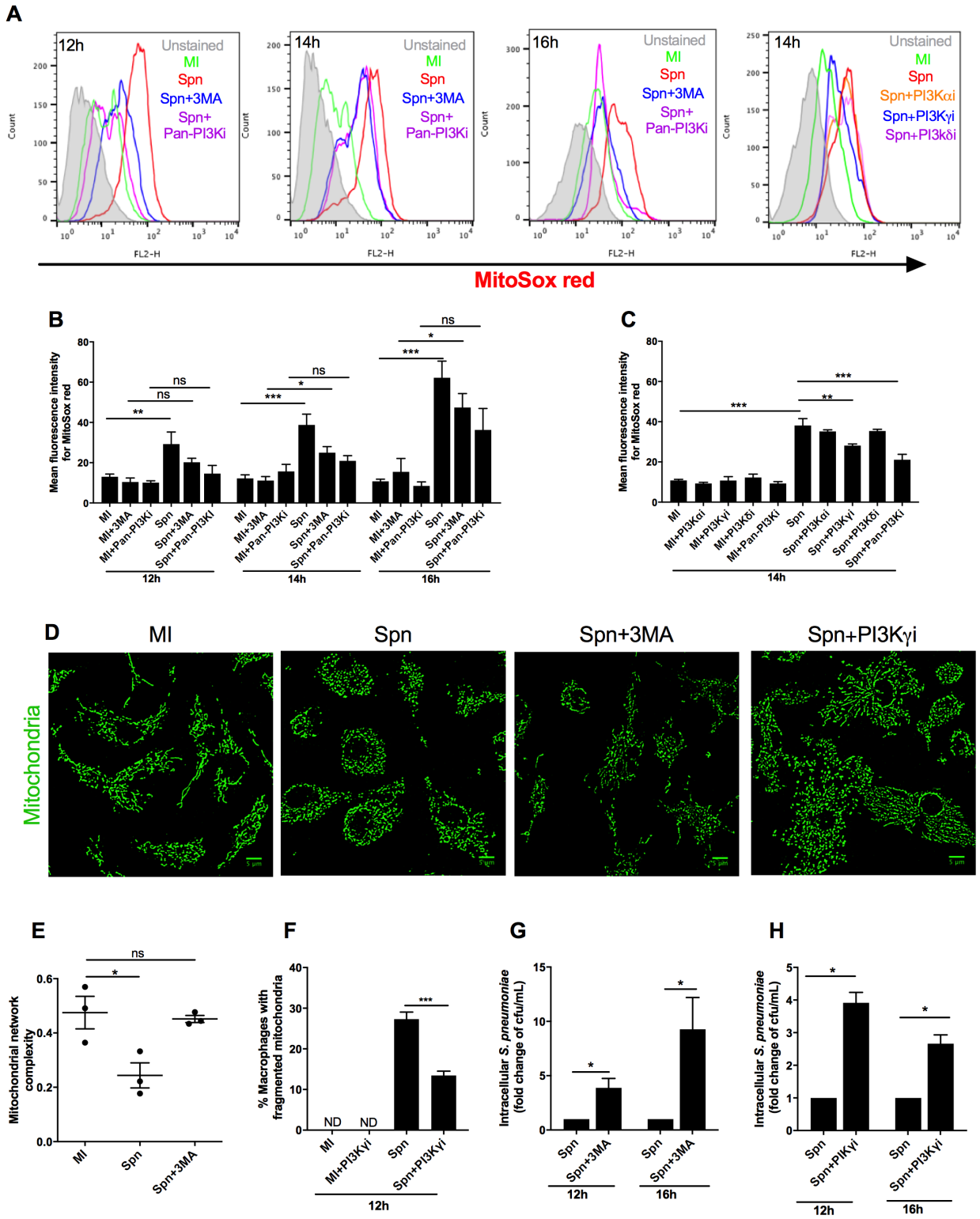

847

848 **Fig 4. PI3K signaling enhances mROS generation and mitochondrial fission.** BMDMs were

849 mock-infected (MI) or challenged with *S. pneumoniae* (Spn) for 12-16 h in the presence of

850 vehicle control or the indicated PI3K inhibitors (3 Methyladenine (3MA), Ly294002 (Pan-
851 PI3Ki), and selective inhibitors of PI3Kα (PI3Kαi), PI3Kγ (PI3Kγi) or PI3Kδ (PI3Kδi) isoforms.
852 (A-C) Cells were stained with MitoSOX Red and analyzed by flow cytometry; (A) shows
853 representative histograms, and mean fluorescence intensity was calculated after PI3K inhibition,
854 n=8 (B) or isoform selective PI3K inhibition, n=3 (C). BMDMs after 12 h of bacterial challenge
855 were stained with anti-TOMM20 to analyze mitochondrial structure. (D) Representative filtered
856 confocal images, scale bars = 5 μm, from one of three independent experiments and
857 mitochondrial network complexity after PI3K inhibition, (E), n=3, and percentage macrophages
858 with fragmented mitochondria after PI3Kγ inhibition (F), n=3 are illustrated. BMDMs were also
859 lysed at selected time points and viable intracellular bacteria (cfu/ml) determined in the presence
860 of 3MA (G), (n=6) or the PI3Kγ inhibitor (H) (n=3) and represented as fold change versus
861 vehicle treatment at each time point. Data are shown as mean±SEM and statistical analysis was
862 performed with one-way ANOVA and Sidak's post-hoc test and student paired *t* test for pair-
863 wise comparison between two-time points. *$p<0.05$, **$p<0.01$, ***$p<0.0001$, ns- non-
864 significant.

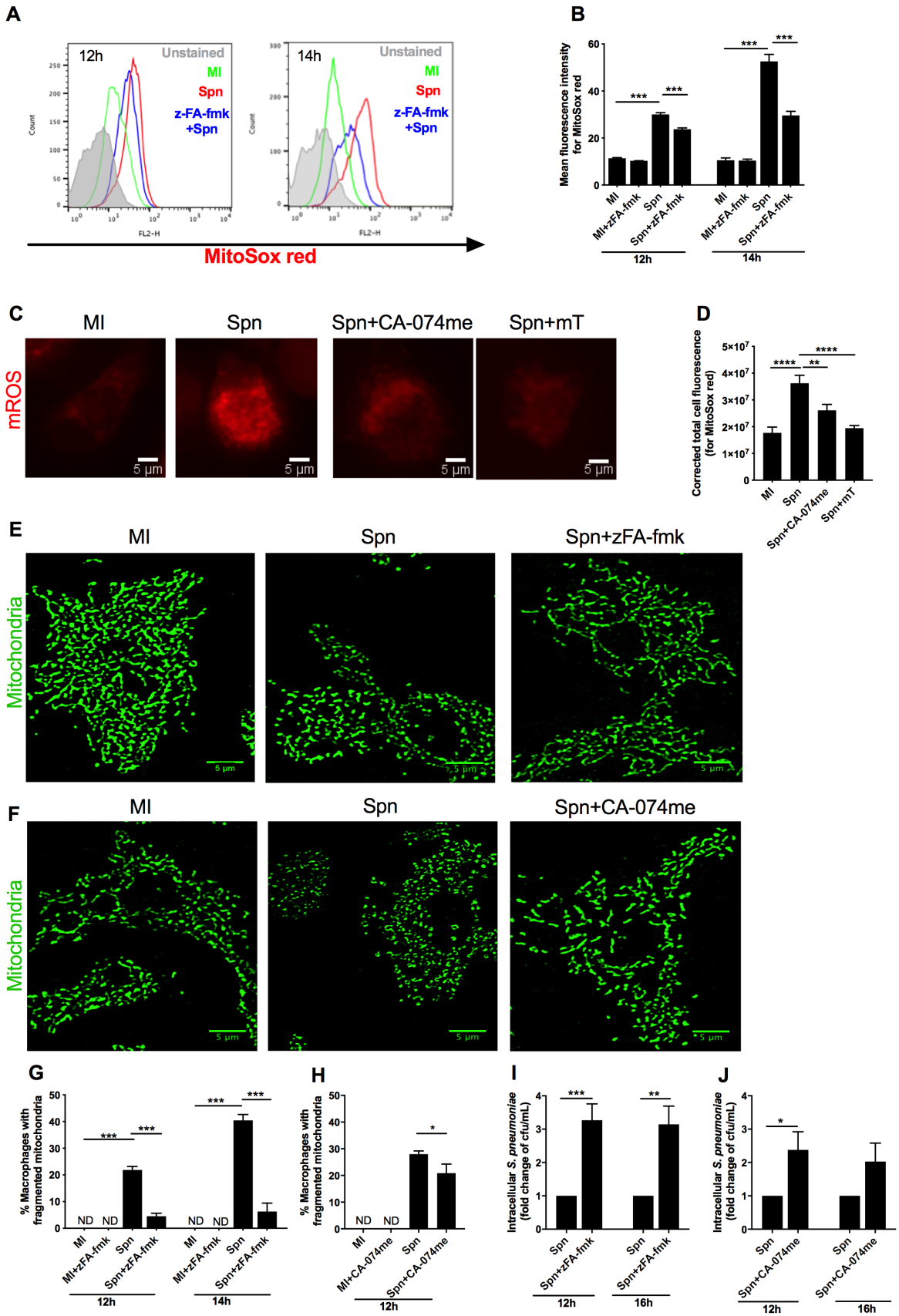
A
12h
Unstained
MI
Spn
z-FA-fmk
+Spn
14h
Count
FL2-H
MitoSox red
B
Mean fluorescence intensity for MitoSox red
MI
MI+zFA-fmk
Spn
Spn+zFA-fmk
12h
14h
C
MI
Spn
Spn+CA-074me
Spn+mT
mROS
5 µm
D
Corrected total cell fluorescence (for MitoSox red)
E
Spn+zFA-fmk
Mitochondria
F
Spn+CA-074me
G
% Macrophages with fragmented mitochondria
ND
H
MI+CA-074me
I
Intracellular S. pneumoniae (fold change of cfu/mL)
16h
J

865

866 **Fig 5. Cathepsin B inhibition modifies mROS generation and mitochondrial fragmentation.**
867 BMDMs were mock-infected (MI) or challenged with *S. pneumoniae* (Spn) for 12-14 h in the
868 presence of vehicle control, zFA-fmk or CA-074me. Cells were stained with MitoSOX Red and
869 either analysed by flow cytometry (A-B) or confocal microscopy (C-D). Representative
870 histograms are shown (A) or mean fluorescence intensity plotted (n=4) (B) 12-14h after bacterial
871 challenge in the presence or absence of zFA-fmk treatment. For 14h after bacterial challenge in
872 the presence or absence of CA-074me treatment, representative unprocessed images are shown
873 (C) and (D) corrected total cell fluorescence was calculated, (n=4). BMDMs were stained with
874 anti-TOMM20 (green) and percentage of macrophages with fragmented mitochondria was
875 measured at the indicated time-points 12-14h after bacterial challenge in the presence or absence
876 of zFA-fmk (E, G) or CA-074me (F, H) and representative filtered confocal images, scale bars =
877 5 µm, from three independent experiments for zFA-fmk (E) and CA-074me (F) at 12 h are
878 shown. Percentage macrophages with fragmented mitochondria 12-14h after bacterial challenge
879 in the presence or absence of zFA-fmk treatment (G), (n=3) or 12h after bacterial challenge in
880 the presence or absence of CA-074me (H), (n=3) are depicted. BMDMs challenged with bacteria
881 for 12-16h in the presence or absence of zFA-fmk were lysed, viable intracellular bacteria
882 (cfu/ml) were calculated and the fold change estimated in the presence of zFA-fmk (as compared
883 to vehicle treatment) (I) (n=6) or were challenged with bacteria for 12-16 h in the presence or
884 absence of CA-074me, cfu/ml calculated and the fold change estimated after CA-074me
885 treatment (as compared to vehicle control) (J) n=3. Data are shown as mean ± SEM. Statistical
886 analysis was performed with one-way ANOVA with Sidak's multiple comparison test and
887 student paired *t* test for pair-wise comparison **p=0.01, ***p<0.001.

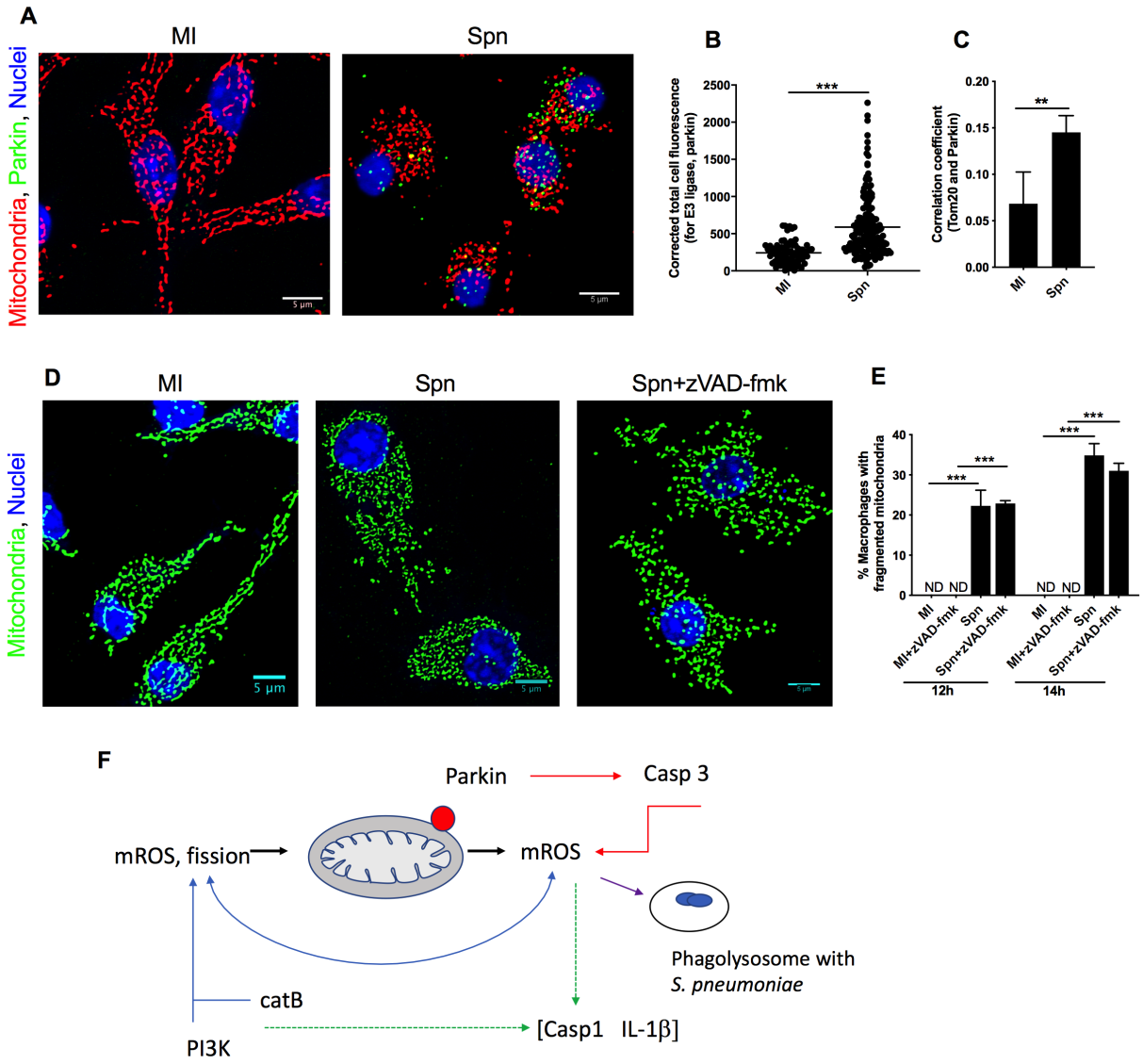

Fig 6. Mitochondrial Parkin recruitment occurs in association with mitochondrial fragmentation before apoptosis. BMDMs were mock-infected (MI) or challenged with *S. pneumoniae* (Spn) for 12 h and stained with anti-TOMM20 (red) to outline mitochondria and with anti-Parkin antibody (green). (A) Representative filtered confocal images, scale bars = 5 µm, from one of three independent experiments are shown. (B) Corrected total cell fluorescence for Parkin was calculated for 78 (MI) or 176 (Spn) BMDMs across three independent experiments and (C) a correlation coefficient was calculated between TOMM20 stained

896 mitochondria and Parkin, (n=3). Data are shown as mean ± SEM. Statistical analyses were
897 performed by paired t-tests. BMDMs (MI or Spn) were also challenged for 12-16 h in the
898 presence or absence of zVAD-fmk and then stained with anti-TOMM20 (green) to outline
899 mitochondrial structure. (D) Representative filtered confocal images of mitochondrial
900 complexity at 12 h, scale bars = 5 μm, from one of three independent experiments are shown and
901 (E) the percentage of macrophages with fragmented mitochondria at 12-14 h are shown, (n=3).
902 Data are shown as mean ± SEM. Statistical analysis was performed with one-way ANOVA with
903 Sidak's multiple comparison. **$p<0.01$, ***$p<0.001$. (F) Schematic Figure illustrating that
904 increased production of mitochondrial ROS (mROS) occurs following increased fission and
905 showing this occurs upstream of subsequent Parkin activation, caspase 3 (Casp3) activation,
906 which further enhances mROS production. Caspase 1 (Casp1) activation and IL-1β production is
907 enhanced by mROS production and cathepsin B (CatB) activation but is downstream of fission
908 and is not related to apoptosis. Phosphoinositide 3-kinase (PI3K) signalling also induces
909 mitochondrial fission and mROS production.
910
911
912
913
914
915
916
917
918

SUPPORTING INFORMATION

A

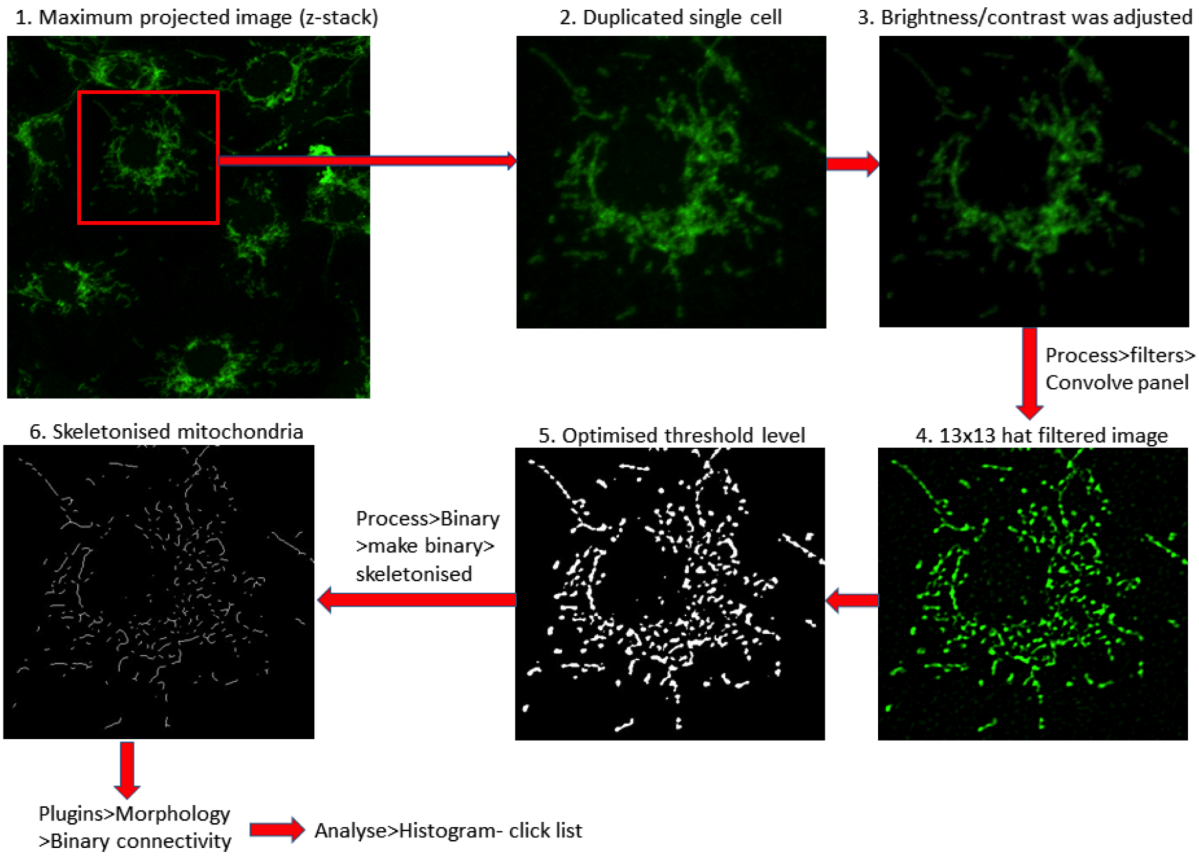

B

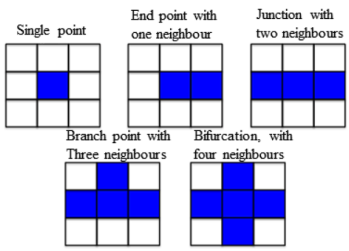

Value (WT-Mock infected)	Count	Description	Network complexity
0	62232	Background	Ratio of total number of Branch points(value ≥4) and End points(value =2) (187+33+3)/322= 0.69
1	4	Single pixels	
2	322	End points	
3	1708	Junction with two neighbours (more count higher the length)	
4	187	Triple point with three neighbour (Branch point)	
5	33	Bifurcation with four neighbours (Branch point)	
6	3	Five neighbours (branch point)	

921 **Fig S1. Schematic of calculation of mitochondrial network complexity using the binary**
922 **connectivity and morphology plug-in of ImageJ.**
923 (A) Schematic diagram illustrating method used to calculate the mitochondrial network
924 complexity of the total population of mitochondria in each cell. Each cell was selected and
925 duplicated from the maximum projected image. The resolution of each cell was enhanced using a
926 13 x 13 hat filter before threshold level correction was performed. The total population of
927 mitochondria in each cell was skeletonized using a binary plugin. The voxel or mitochondrial
928 connectivity was evaluated by the binary connectivity of morphology plug-in in ImageJ. The
929 network complexity is defined as the ratio of total branch points and total end points. (B)
930 Representative calculation of a single cell's mitochondrial network complexity. The left
931 rectangles show how the voxel connectivity were quantified using the binary connectivity plugin
932 and the table defines each value used and how the ratio of total branch points and total end points
933 was calculated from the binary pixels.
934

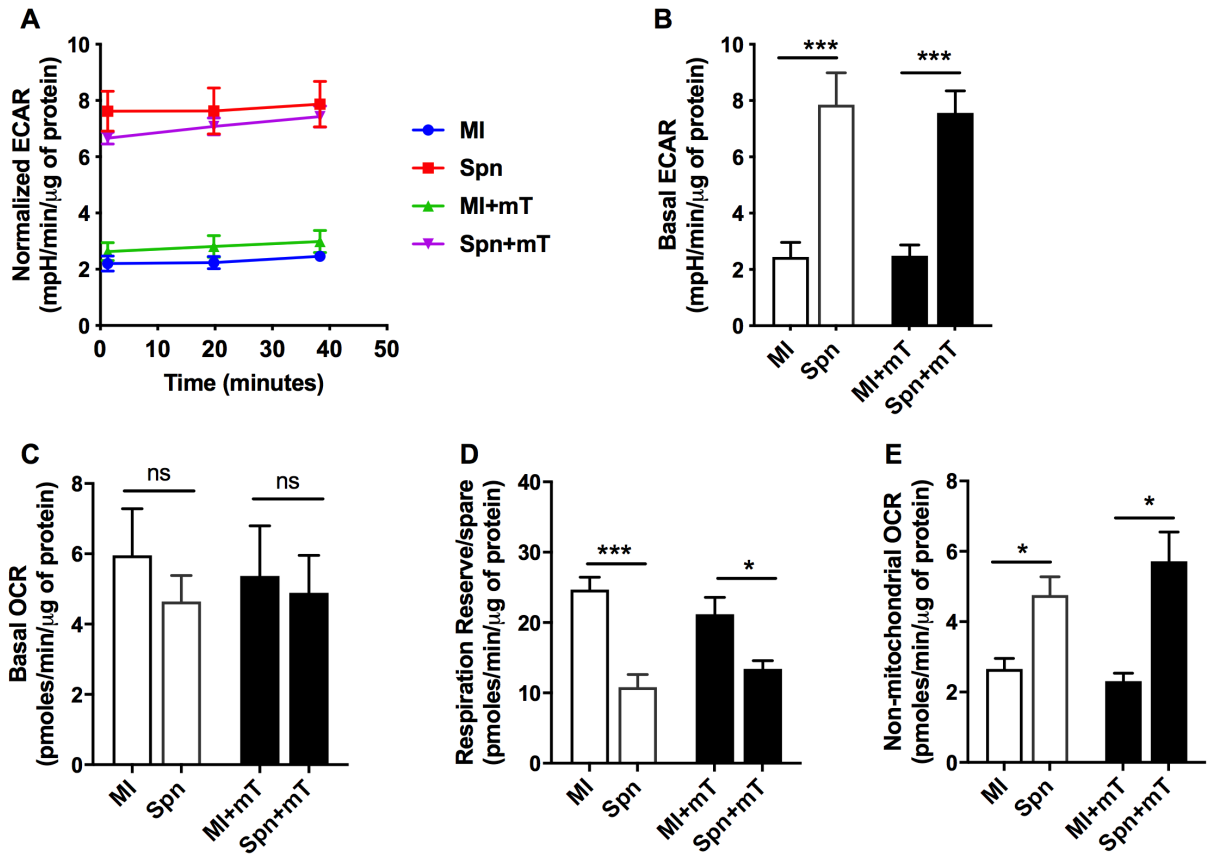

935

936 **Fig S2. Metabolic profile of BMDMs following *S. pneumoniae* challenge**.

937 BMDMs were mock-infected (MI) or challenged with *S. pneumoniae* (Spn) for 12 h in the

938 presence of pre-treatment with the mROS inhibitor MitoTempo (+mT) or vehicle control.

939 Subsequently, the extracellular acidification rate (ECAR) and mitochondrial oxygen

940 consumption rate (OCR) were measured by the Seahorse X24 extracellular flux analyser in the

941 same experiments as Figure 3. The normalized ECAR (A), basal ECAR (B), basal OCR (C),

942 respiration reserve (D) and non-mitochondrial OCR (E) were calculated. Data are shown as mean

943 ± SEM, n=4. Statistical analysis was performed with one-way ANOVA with Sidak's post-hoc

944 test for multiple comparisons, *$p \leq 0.05$, ***$p \leq 0.001$.

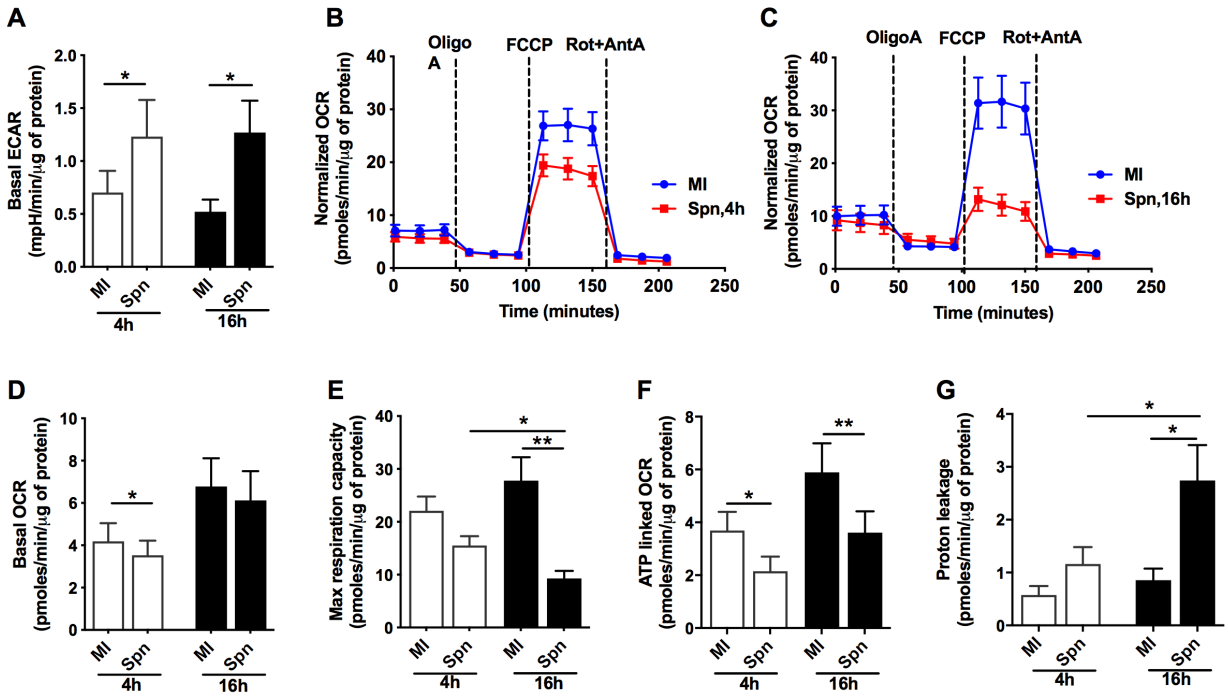

Fig S3. Metabolic profile of MDMs following *S. pneumoniae* challenge.

Human monocyte-derived macrophages (MDMs) were mock-infected (MI) or challenged with *S. pneumoniae* (Spn) for 4 or 16 h and the extracellular acidification rate (ECAR) and mitochondrial oxygen consumption rate (OCR) was measured by the Seahorse X24 extracellular flux analyser. (A) Basal ECAR, (B) representative plots for the OCR kinetic data at 4 h and (C) at 16 h, (D) basal OCR, (E) maximum respiration capacity, (F) ATP-linked OCR and (G) proton leakage were calculated. Data are shown as mean ± SEM, n=5 (4 h) and n=6 (16 h). Statistical analysis was performed with one-way ANOVA with Sidak's post-hoc test for multiple comparisons, *$p \leq 0.05$, ***$p \leq 0.001$.

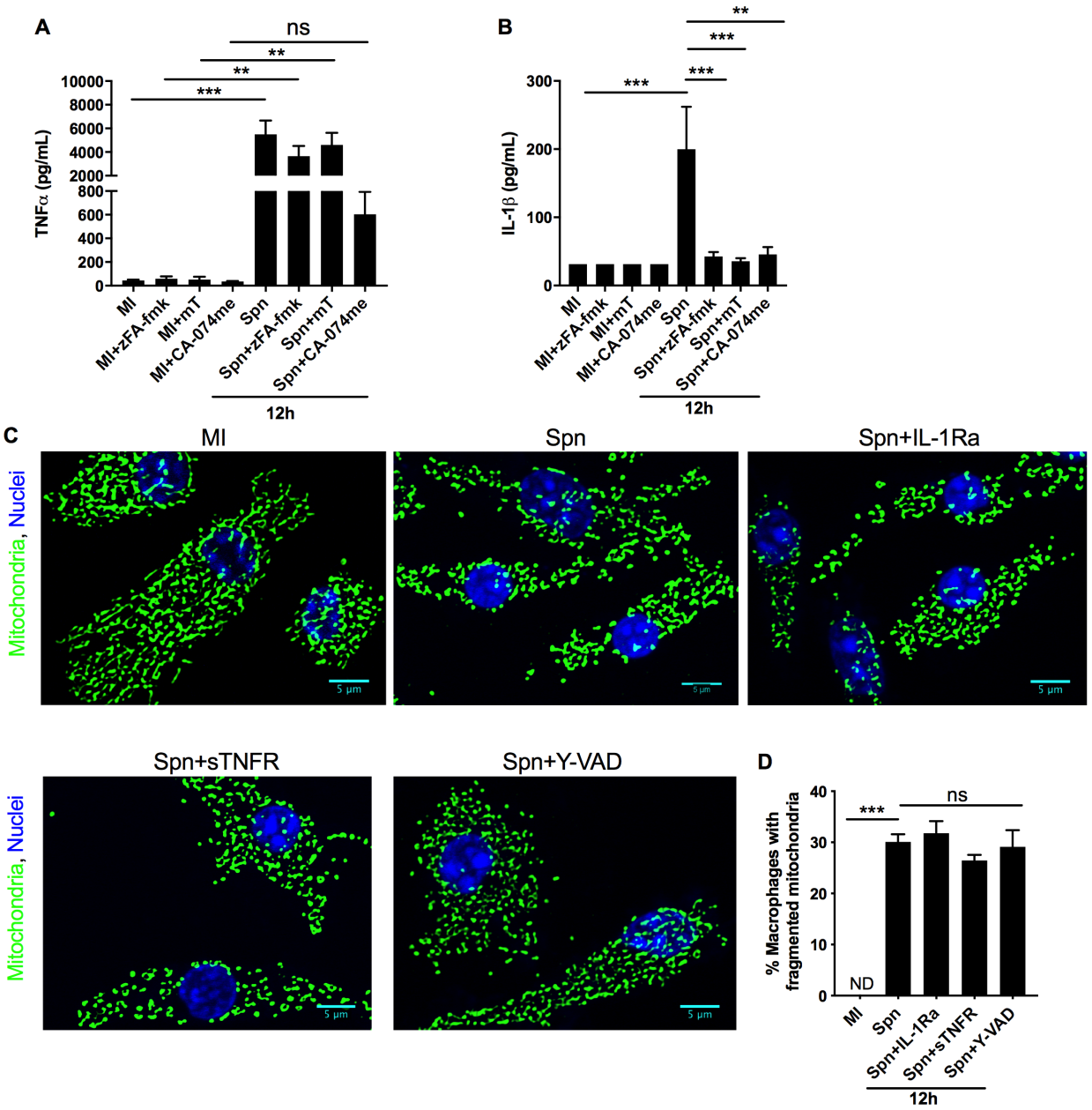

955

956 **Fig S4. IL-1β production is regulated by mROS but does not regulate mitochondrial**

957 **fission.** BMDMs were mock-infected (MI) or challenged with *S. pneumoniae* (Spn) for 12 h in

958 the presence or absence of pre-treatment with the cathepsin B inhibitors zFA-fmk or CA-047me

959 or the mROS inhibitor MitoTempo (mT) and supernatants collected for assessment of (A)

960 TNFα, n=6 or (B) IL-1β by ELISA, n=4. BMDMs were mock-infected (MI) or challenged with

961 *S. pneumoniae* (Spn) for 12 h in the presence or absence of pre-treatment with IL-1RA, sTNFR1
962 or the caspase 1 inhibitor YVAD and cells stained with anti-TOMM20 and mitochondrial
963 complexity calculated. (C) Representative filtered confocal images, from three independent
964 experiments are shown and (D) the percentage of macrophages with fragmented mitochondria
965 shown, n=3, scale bars = 5 μm. Data are shown as mean ± SEM. Statistical analysis was
966 performed with one-way ANOVA with Sidak's post-hoc test for multiple comparisons, *$p \leq 0.05$,
967 **$p \leq 0.01$. ***$p \leq 0.001$.

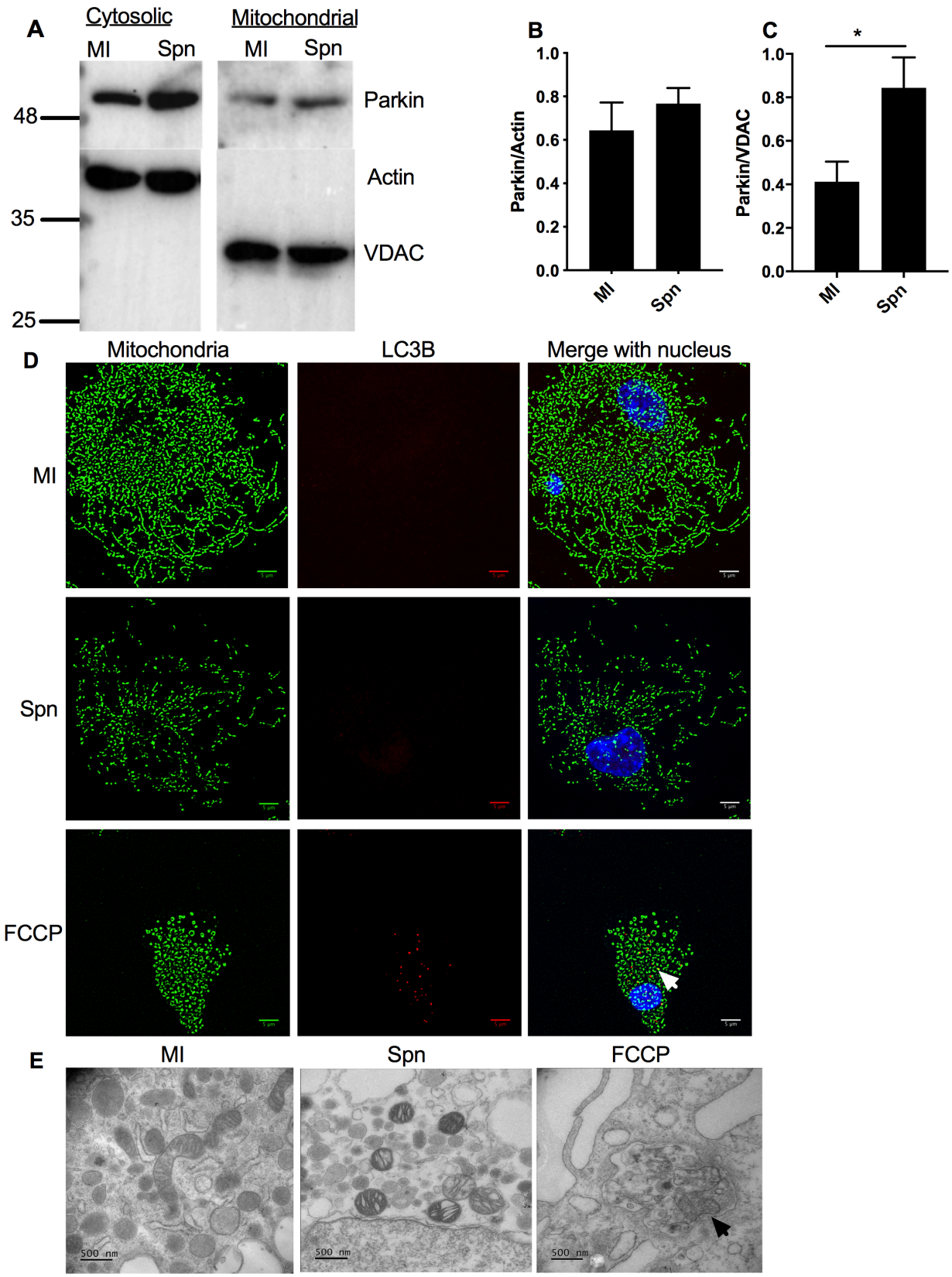
A
Cytosolic
Mitochondrial
MI
Spn
MI
Spn
48
35
25
Parkin
Actin
VDAC
B
Parkin/Actin
1.0
0.8
0.6
0.4
0.2
0.0
MI
Spn
C
*
Parkin/VDAC
1.0
0.8
0.6
0.4
0.2
0.0
MI
Spn
D
Mitochondria
LC3B
Merge with nucleus
MI
Spn
FCCP
E
MI
Spn
FCCP
500 nm
500 nm
500 nm

968

969 **Fig S5. Parkin recruitment to mitochondria is not associated with mitophagy.** BMDMs were
970 mock-infected (MI) or challenged with *S. pneumoniae* (Spn) for 12 h and cells were lysed and
971 fractionated into cytosolic and mitochondrial fractions. (A) A representative western blot after
972 probing with anti-Parkin antibody is shown, with actin used as a cytosolic loading control and
973 voltage dependent anion channel (VDAC) as a mitochondrial loading control. The blot is
974 representative of three independent experiments. Densitometry was performed to estimate the
975 (B) Parkin/actin and (C) Parkin/VDAC ratios, n=3. Data are shown as mean ± SEM. Statistical
976 analysis was performed with student paired *t* test for pair-wise comparisons. (D) BMDMs were
977 MI or challenged with Spn or exposed to Carbonyl cyanide 4-(trifluoromethoxy)
978 phenylhydrazone (FCCP; positive control). After 12 h BMDMs were harvested and stained with
979 anti-TOMM20 (green) to outline mitochondrial structure or with anti-LC3B (red) as marker of
980 mitophagy. A representative filtered image from three independent experiments is shown, scale
981 bars = 5 μm. (E) Under the same conditions macrophages were harvested and examined by
982 transmission electron microscopy to search for double membrane containing vacuoles containing
983 mitochondria consistent with mitophagy (arrowhead), as shown with the positive control FCCP.
984 The images are representative of three independent experiments. Scale bars =500 nm.

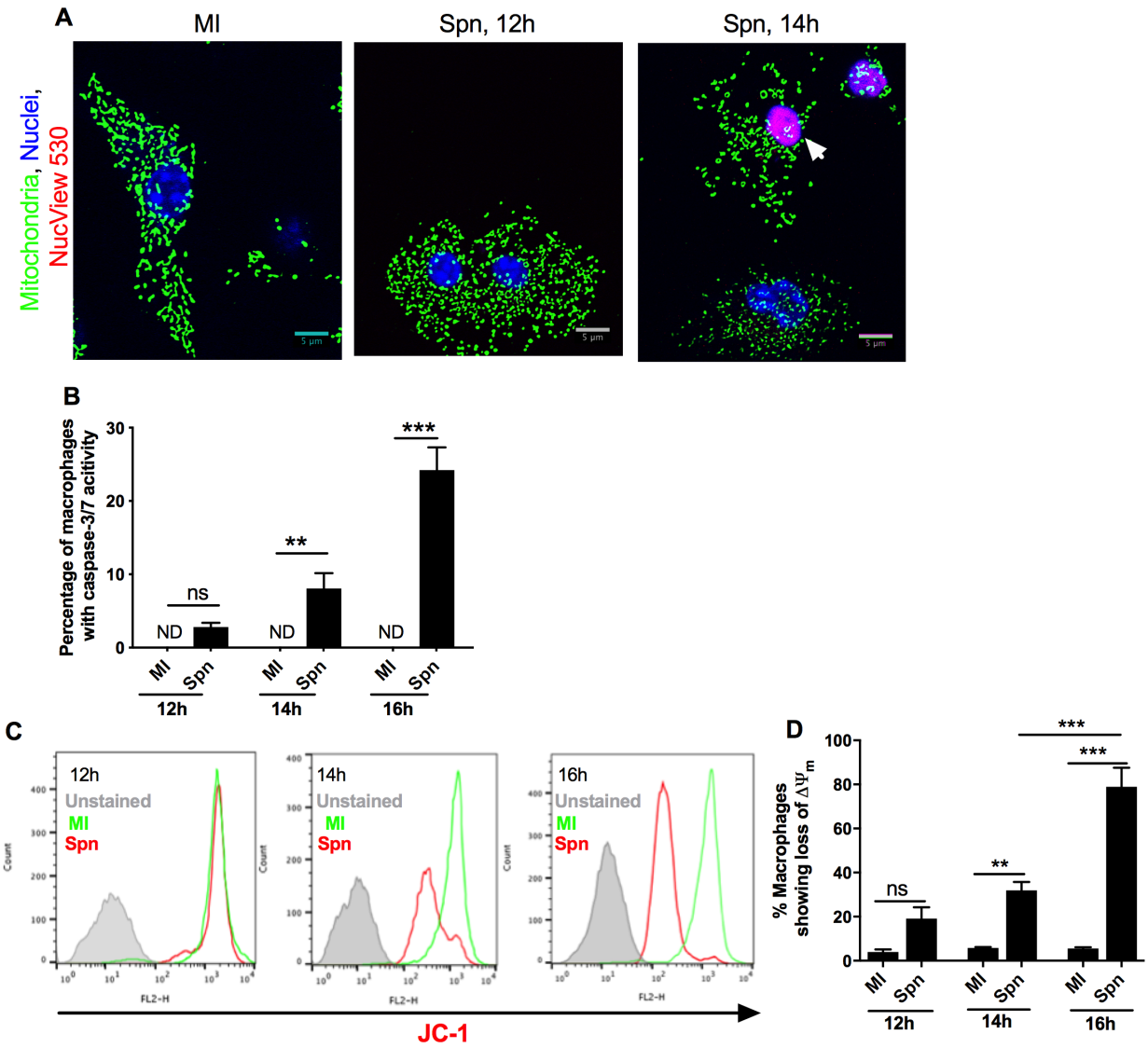

985

986 **Fig S6. Apoptosis of macrophages following bacterial challenge occurs downstream of**

987 **mitochondrial fission.** BMDMs were mock-infected (MI) or challenged with *S. pneumoniae*

988 (Spn) for 12-16 h and cells stained with NucView 530 (red) to detect caspase 3/7 activation

989 during apoptosis and with DAPI (blue) to detect total cell count. Along with NucView red and

990 DAPI staining, cells were also stained with anti-TOMM20 (green) (A) Representative filtered

991 images from three independent experiments are shown, scale bars = 5 µm and (B) quantification

992 of the percentage of caspase 3/7 positive BMDMs, n=3 are shown. Under the same conditions

993 JC-1 staining was performed to measure loss of $\Delta\psi_m$ by flow cytometry. (C) Representative
994 histograms, from three independent experiments, are shown at 12-16 h after challenge with
995 unstained cells in grey, MI in green and Spn exposed BMDMs in red. (D) The percentage of
996 BMDMs showing loss of $\Delta\psi_m$ at each time point are shown, n=3. Data are shown as mean ±
997 SEM. Statistical analysis was performed with one-way ANOVA with Sidak's post-hoc test for
998 multiple comparisons, *$p \leq 0.05$, **$p \leq 0.01$. ***$p \leq 0.001$.

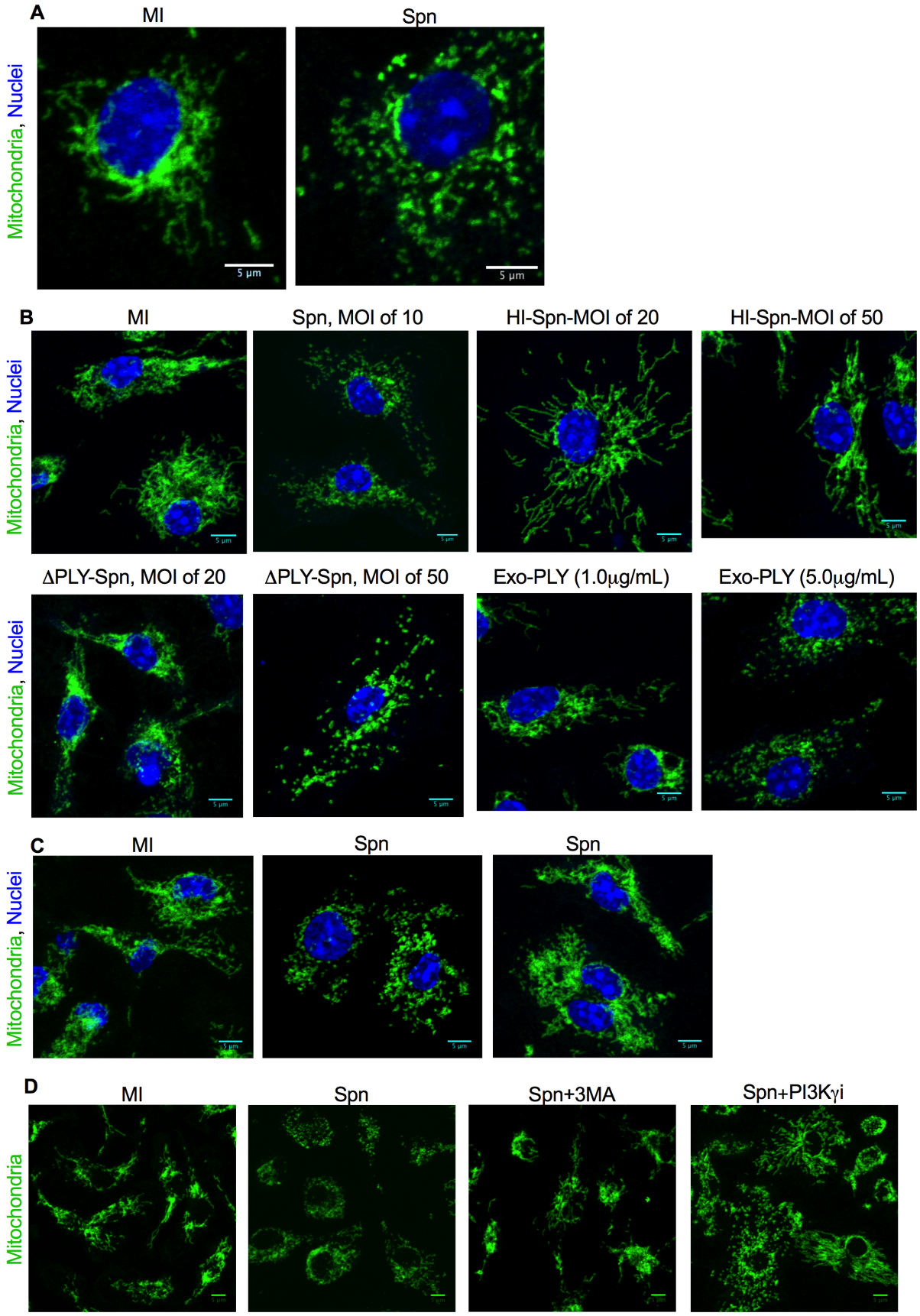
A
MI
Spn
Mitochondria, Nuclei
5 µm
5 µm
B
MI
Spn, MOI of 10
HI-Spn-MOI of 20
HI-Spn-MOI of 50
Mitochondria, Nuclei
ΔPLY-Spn, MOI of 20
ΔPLY-Spn, MOI of 50
Exo-PLY (1.0µg/mL)
Exo-PLY (5.0µg/mL)
Mitochondria, Nuclei
C
MI
Spn
Spn
Mitochondria, Nuclei
D
MI
Spn
Spn+3MA
Spn+PI3Kγi
Mitochondria

999

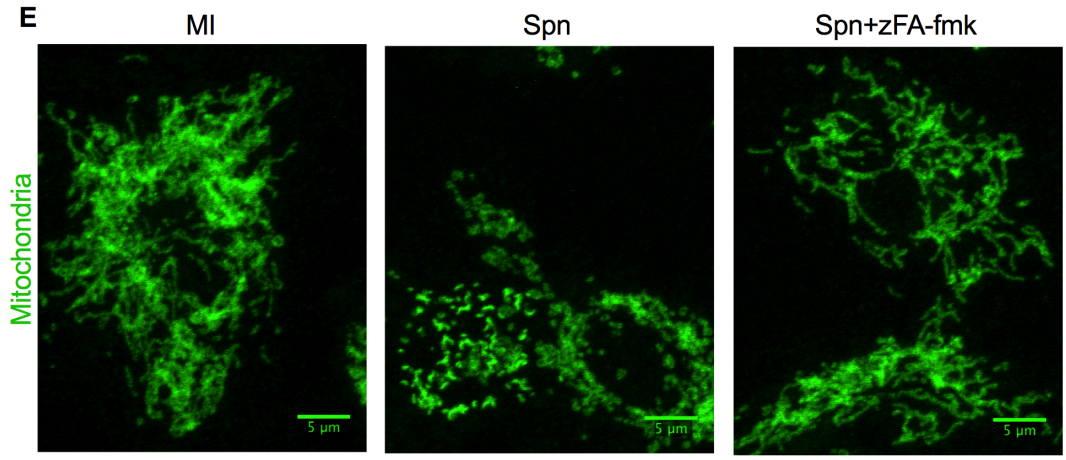
E
MI
Spn
Spn+zFA-fmk
Mitochondria
5 µm
5 µm
5 µm

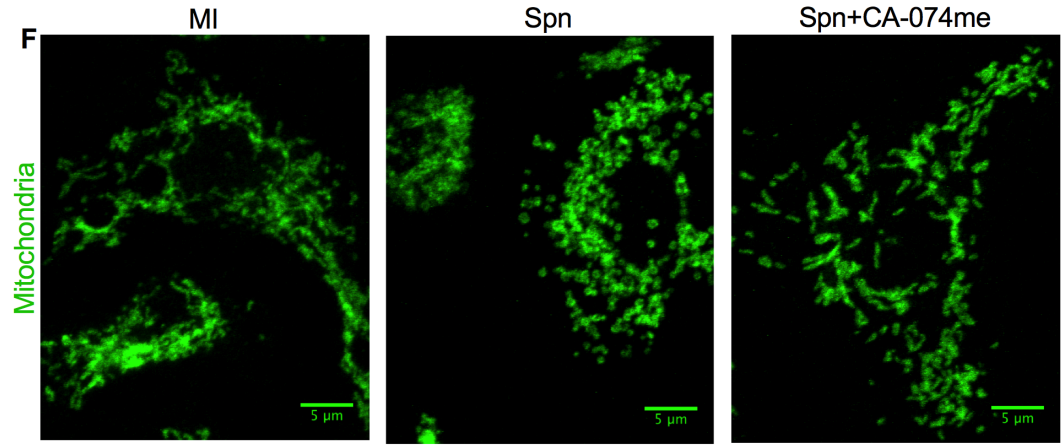
F
MI
Spn
Spn+CA-074me
Mitochondria
5 µm
5 µm
5 µm

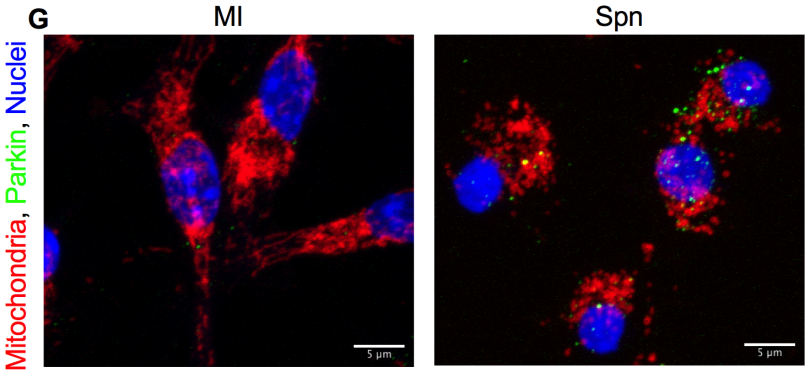
G
MI
Spn
Mitochondria, Parkin, Nuclei
5 µm
5 µm

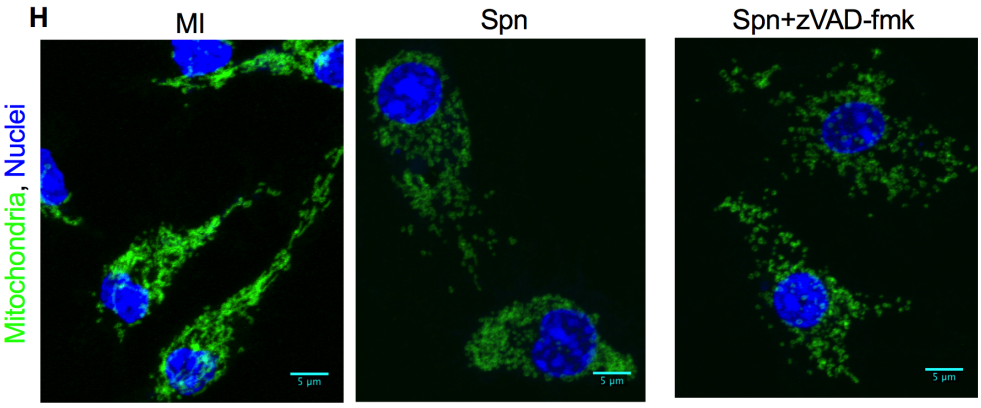
H
MI
Spn
Spn+zVAD-fmk
Mitochondria, Nuclei
5 µm
5 µm
5 µm

1000

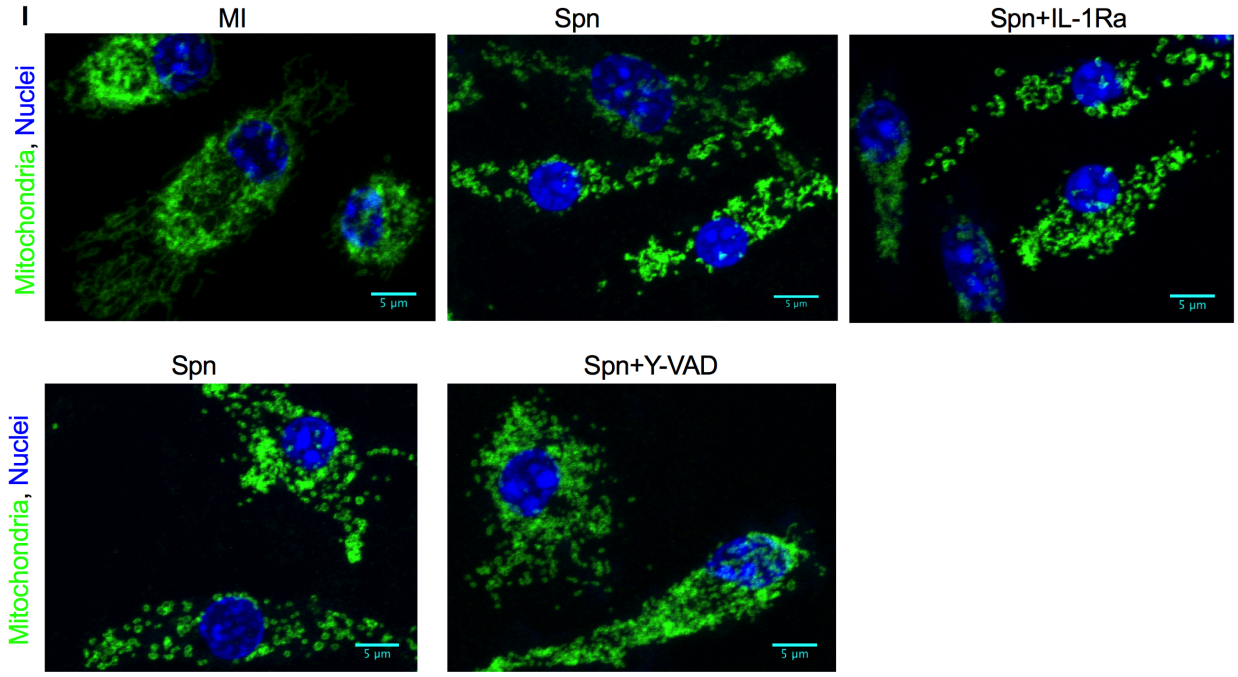
I
MI
Spn
Spn+IL-1Ra
Mitochondria, Nuclei
5 µm
Spn
Spn+Y-VAD
Mitochondria, Nuclei
5 µm

1001

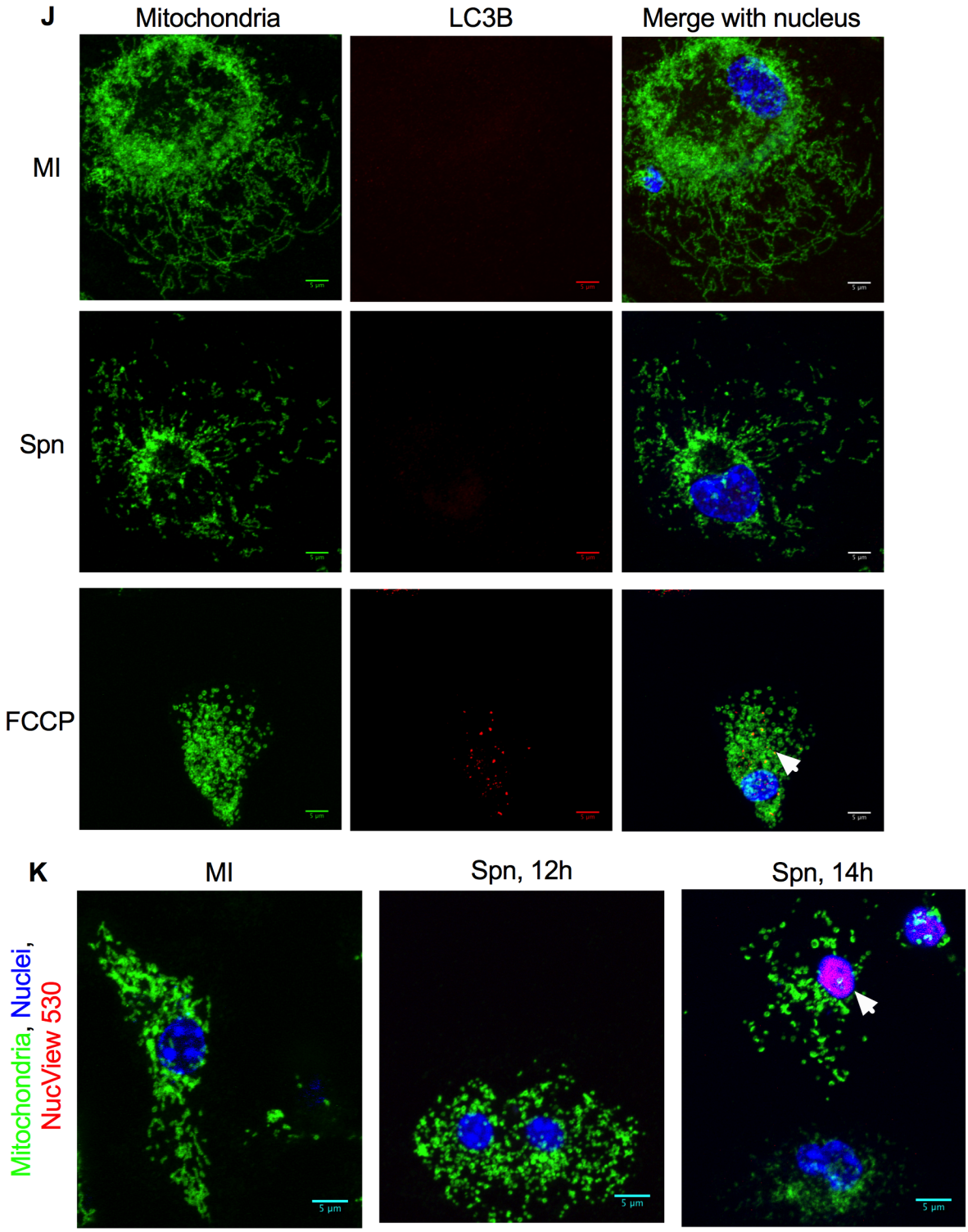

1002

1003 **Fig S7. Unfiltered confocal images used to generate the filtered images shown in the**

1004 **manuscript.** Images were generated using bone marrow derived macrophages (BMDMs) that

1005 were mock-infected (MI) or exposed to *S. pneumoniae* (Spn) at a MOI of 10, for 12 h, unless
1006 otherwise stated, in the presence or absence of various inhibitors and vehicle controls and then
1007 stained as described in each individual Figure legend. Representative unprocessed images
1008 generated by confocal microscopy are depicted and represent the images used to generate the
1009 indicated filtered images shown throughout the text. Scale bars = 5 μm unless otherwise stated
1010 (A) MI or Spn BMDM stained with the mitochondrial outer membrane specific marker
1011 TOMM20 (green) to delineate mitochondrial structure. The unprocessed images correspond to
1012 the images Fig. 1A. (B) MI or Spn BMDMs or those exposed to heat-inactivated Spn (HI-Spn) or
1013 a pneumolysin deficient Spn mutant (ΔPLY Spn), at the indicated multiplicity of infection, or
1014 exogenous pneumolysin (0.5 μg/mL-5 μg/mL) were stained with anti-TOMM20 (green) or
1015 Draq5 staining to label nuclei (blue). Unprocessed images represent the images as shown in Fig.
1016 2A. (C) MI or Spn BMDM were pre-treated with mROS inhibitor MitoTempo (+mT) or vehicle
1017 control before staining with anti-TOMM20 (green) and Draq5 (blue). Unprocessed images
1018 represent the images as shown in Fig. 3H. (D) MI or Spn BMDMs were challenged in the
1019 presence of vehicle control or the indicated PI3K inhibitors (3 Methyladenine (3MA), Ly294002
1020 (Pan-PI3Ki), and selective inhibitors of PI3Kα (PI3Kαi), PI3Kγ (PI3Kγi) or PI3Kδ (PI3Kδi)
1021 isoforms and stained with anti-TOMM20 (green) staining. Representative unprocessed images
1022 represent the images shown in Fig. 4D. (E,F) MI or Spn BMDMs were challenged in the
1023 presence of vehicle control, zFA-fmk (E) or CA-074me (F). Cells were stained with anti-
1024 TOMM20 (green) and representative unprocessed images represent the images shown in Fig. 5E
1025 (E) and Fig. 5F (F). (G) MI or Spn BMDMs were stained with anti-TOMM20 (red), Draq5 (blue)
1026 and anti-Parkin antibody (green). Representative unprocessed confocal images correspond to Fig.
1027 6A. (H) MI or Spn BMDMs in the presence or absence of zVAD-fmk were stained with anti-

1028 TOMM20 (green). Representative unprocessed confocal images correspond to Fig. 6D. (I) MI or
1029 Spn BMDMs in the presence or absence of pre-treatment with IL-1RA, sTNFR1 or the caspase 1
1030 inhibitor YVAD were stained with anti-TOMM20 (green) and Draq5 (blue). Representative
1031 unprocessed images were those used in Fig. S5C. (J) MI or Spn BMDMs or BMDM exposed to
1032 FCCP (positive control) were stained with anti-TOMM20 (green), Draq5 (blue) or with anti-
1033 LC3B (red). Representative unprocessed images correspond to those used in Fig. S6D. (K) MI or
1034 Spn BMDMs at the indicated time points were stained with anti-TOMM20 (green), NucView
1035 530 (red) to detect caspase 3/7 activation during apoptosis and with DAPI (blue) to stain nuclei.
1036 Representative unprocessed images correspond to those used in Fig. S7A.